

Inference of cosmological models with principal component analysis

Ranbir Sharma^{1,*} and H K Jassal¹

¹Indian Institute of Science Education and Research Mohali, Punjab, 140306, India.

*Corresponding author. E-mail: ranbirsharma0313@gmail.com

Abstract. Determination of cosmological parameters is a major goal in cosmology at present. The availability of improved data sets necessitates the development of novel statistical tools to interpret the inference from a cosmological model. In this paper, we combine the Principal Component Analysis (PCA) and Markov Chain Monte Carlo (MCMC) method to infer the parameters of cosmological models. We use the No U-Turn Sampler (NUTS) to run the MCMC chains in the model parameter space. After determining the observable by PCA, we replace the observational and error parts of the likelihood analysis with the PCA reconstructed observable and find the most preferred model parameter set. As a demonstration of our methodology, we assume a polynomial expansion as the parametrization of the dark energy equation of state and plug it in the reconstruction algorithm as our model. After testing our methodology with simulated data, we apply the same to the observed data sets, the Hubble parameter data, Supernova Type Ia data, and the Baryon Acoustic oscillation data. This method effectively constrains cosmological parameters from data, including sparse data sets.

Keywords. Cosmology—(dark energy equation of state reconstruction)—(Principal Component Analysis)—(correlation coefficient)

1. Introduction

Observational evidence of the acceleration of the Universe marked the beginning of a new era in Cosmology. It is well established that the current expansion of the Universe is accelerating, and an explanation for the current acceleration is done by way of introducing the Dark Energy(DE) term in the Einstein equation. Dark energy is described by its equation of state parameter (EoS) $w = -P'/\rho'$, where ρ' is the energy density and P' is its pressure contribution. It is still unknown whether dark energy is a cosmological constant (Carroll *et al.*, 1992; Carroll, 2001; Turner & White, 1997; Padmanabhan, 2003) or a time-evolving entity (Peebles & Ratra, 2003; Copeland *et al.*, 2006). The Λ CDM (*cosmological constant and cold dark matter*) model corresponds to the dark energy equation of state value $w = -1$, whereas in the case of time-evolving dark energy, the dark energy equation of state parameter varies with time and can assume different values of w (Padmanabhan, 2003; Peebles & Ratra, 2003; Carroll *et al.*, 1992; Weinberg, 1989; Coble *et al.*, 1997; Caldwell *et al.*, 1998; Sahni & Starobinsky, 2000; Ellis, 2003; Linder, 2008; Frieman *et al.*, 2008; Albrecht *et al.*, 2006; Stern *et al.*, 2010; Arjona & Nesseris, 2020). Various models based on scalar, canonical, and non-canonical fields have been proposed to overcome different problems of Λ CDM model (Ratra & Peebles, 1988; Linder, 2006; Caldwell & Linder, 2005; Linder, 2008; Huterer

& Peiris, 2007; Zlatev *et al.*, 1999; Copeland *et al.*, 1998; Padmanabhan, 2002; Singh *et al.*, 2019; Bagla *et al.*, 2003; Tsujikawa, 2013; Rajvanshi & Bagla, 2019; Chevallier & Polarski, 2001). The discrepancies in H_0 measurements and its implication in cosmological model selection is discussed in Banerjee *et al.* (2021) and Lee *et al.* (2022). The last two decades have also marked the era of precision Cosmology. Cosmological parameters are measured to high precision utilizing the availability of new data-sets (Planck Collaboration *et al.*, 2018; Chevallier & Polarski, 2001; Sangwan *et al.*, 2018).

Maximum Likelihood Estimation analysis(MLE) is the most commonly used technique in cosmological parameter estimation(Singh *et al.*, 2019; Jassal, 2009; Nesseris & Perivolaropoulos, 2004, 2005, 2007; Sangwan *et al.*, 2018). The increasing availability of the observational data-set has tightened the constraints on the parameters of theoretical models (Chevallier & Polarski, 2001; Linder, 2003; Jassal *et al.*, 2005; Gong & Wang, 2007; Mukherjee, 2016; Vagnozzi *et al.*, 2018; Di Valentino *et al.*, 2017; Bellomo *et al.*, 2020; Bernal *et al.*, 2020; Verde *et al.*, 2013). Though it is crucial to determine the theory parameters, we have the observational data dependencies in the core of these methods, and new data sets reject or accept a particular model with quantified precision. Methods like the Principal Component Analysis (PCA) enable us to determine the functional form of the observable of a data-set in a

model independent, non-parametric manner (Huterer & Starkman, 2003; Huterer & Cooray, 2005; Zheng & Li, 2017; Ishida & de Souza, 2011; Crittenden *et al.*, 2009; Clarkson & Zunckel, 2010; Miranda & Dvorkin, 2018; Sharma *et al.*, 2020; Hart & Chluba, 2019; Nesseris & García-Bellido, 2013; Nair & Jhingan, 2013; Hojjati *et al.*, 2012; Hart & Chluba, 2022a). PCA is a multivariate analysis that gives the form of cosmological quantities as a function of redshift (Huterer & Starkman, 2003; Clarkson & Zunckel, 2010; Huterer & Cooray, 2005; Zheng & Li, 2017; Sharma *et al.*, 2020). In a previous work (Sharma *et al.*, 2020), we combined PCA and Correlation Coefficient Calculation to give the analytical, functional form of the observable quantity when observational data-sets are given as input. The method is efficient in fitting the observable; the caveat however is that the derived cosmological parameters like the dark energy equation of state parameter are not determined very efficiently. The problem arises due to the non-linear dependency of the dark energy parameter to the observational quantity at hand, for instance, the Hubble parameter and the distance modulus. To circumvent this problem, we incorporate the Markov Chain Monte Carlo method with PCA reconstruction to derive the equation of state parameters for dark energy and other cosmological parameters. The equation of state parameter is derived by searching for the model that best describes the functional form of the observable determined by the observational data. For the Monte Carlo method, we use the No U-Turn Sampler which is a variant of the Hamilton Monte Carlo method. In this analysis, we show that the constraints on the dark energy equation of state parameters are consistent with the constraints obtained from other methods.

This paper is structured as follows. In section 2., we give a brief review of background cosmology, we describe the reconstruction algorithm along with the No U-turn sampling, followed by section 3. where we describe the results of our algorithm. We describe the distinguishing features of our methodology in section 4.. In section 5. we conclude by summarising the main results of this paper.

2. Reconstruction Methodology

In this section, we first discuss the methodology of the Principal Component Analysis reconstruction (Sharma *et al.*, 2020) and the modification to the algorithm.

2.1 Reconstruction of the functional form of Hubble parameter, distance modulus and angular scale in terms of redshift

For a spatially flat Universe, composed of dark energy and non-relativistic matter, the Hubble parameter is given by,

$$H(z) = H_0 \left[\Omega_m (1+z)^3 + \Omega_{DE} e^{3 \int_0^z \frac{1+w(z')}{1+z'} dz'} \right]^{1/2} \quad (1)$$

The dark energy equation of state parameter $w(z) = P'/\rho'$ can be written as

$$w(z) = \sum_{i=1}^m \alpha_{(i-1)} \mathcal{F}(z)^{(i-1)}, \quad \mathcal{F}(z) = \frac{z}{(1+z)} \quad (2)$$

where H_0 denotes the present-day value of the Hubble parameter and Ω_m, Ω_{DE} are the density parameters for matter and dark energy, respectively. In eqn(2), $m = 2$ corresponds to the Chevallier-Polarski-Linder(CPL) parameterization (Chevallier & Polarski, 2001; Linder, 2003) given by, $w(z) = w_0 + w'z/(1+z)$, w_0 and w' being the present-day values of the equation state parameter and its derivative, respectively. The equation gives the Taylor series expression of the dark energy equation of state parameter in terms of $(1-a)$, where a is the scale factor.

From the functional form of the Hubble parameter, we can reconstruct the dark energy equation of state parameter $w(z)$. Differentiating eqn (1) we get,

$$w(z) = \frac{3h^2 - 2(1+z)hh'}{3h_0^2(1+z)^3\Omega_m - 3h^2}, \quad (3)$$

where h is the reduced Hubble parameter given by $H(z)/100 \text{ km s}^{-1} \text{ Mpc}^{-1}$.

The luminosity distance $d_L(z)$ is given by,

$$d_L(z) = \frac{c}{H_0} (1+z) \int_0^z d_H(z') dz' \quad (4)$$

where d_H , from eq(1) is,

$$d_H(z) = \left(\Omega_m (1+z)^3 + \Omega_x e^{3 \int_0^z \frac{(1+w(z')) dz'}{(1+z')}} \right)^{-1/2} \quad (5)$$

and is related to the distance modulus as

$$\mu(z) = 5 \log \left(\frac{d_L}{1 \text{ Mpc}} \right) + 25 \quad (6)$$

We use the same expression of eqn(2) for the EoS parameter to express $\mu(z)$.

Since $D(z) = (H_0/c)(1+z)^{-1}d_L(z)$, the equation of state parameter in terms of distance is given by

$$w(z) = \frac{2(1+z)D'' + 3D'}{3D'^3\Omega_m(1+z)^3 - 3D'} \quad (7)$$

The Baryon Acoustic Oscillation (BAO) angular scale θ_b is defined in terms of the angular diameter D_A as,

$$\theta_b = \frac{r_{drag}}{(1+z)D_A}. \quad (8)$$

Here, r_{drag} is the sound horizon at the drag epoch.

Following the reconstruction method of Sharma *et al.* (2020), we start by calculating the functional form of the reduced Hubble parameter $h(z)$ and distance modulus $\mu(z)$ directly from the data-set, using Principal Component Analysis. The observable of the given data-set is expressed as a polynomial over an initial basis function, which creates a coefficient space. The dimension of the coefficient space is the same as the number of terms in the initial basis function. We select different patches in the coefficient space and do a χ^2 calculation on each patch. For each patch, we get a minimum value of χ^2 . From these minimum χ^2 values of each patch, we create the PCA data-matrix (\mathcal{D}). We then calculate covariance matrix C of \mathcal{D} , from which the eigenvector matrix \mathcal{E} is calculated. \mathcal{E} is used to diagonalize C and omit the linear correlation of the data matrix. It also creates a new set of basis functions. The observables are finally expressed in terms of the final basis function. With the help of these new basis functions, we create the new data-matrix \mathcal{D}' . To select the value of the final basis number M , we compare the correlation matrix of \mathcal{D} and \mathcal{D}' . Comparison of the correlation matrix also helps us to choose the better initial basis variable.

If the initial basis function is given by

$$G = (f_1(z), f_2(z), \dots, f_N(z)),$$

with $f_i(z) = f(z)^{(i-1)}$, the initial expression of the observable ξ in terms of the independent variable z is given by,

$$\xi_{ini}(z) = \sum_{i=1}^N b_i f(z)^{(i-1)} \quad (9)$$

The value of N is the number of terms in the polynomial expression of $\xi_{ini}(z)$; it is also the dimension of coefficient space \vec{b} . The correlation coefficient calculation determines the value of N (Kendall, 1938; Sharma *et al.*, 2020). This value must be large enough that the

function can capture most of the features from the observed data-set. To select the value of N , we calculate Pearson, Spearman, and Kendall correlation coefficients for the data-matrix \mathcal{D} (Kendall, 1938; Kreyszig *et al.*, 2011). The Pearson correlation coefficient gives the linear correlation that exists in the data-set. On the other hand, Spearman and Kendall correlation coefficients give the non-linear correlations of the data-set. For the Spearman correlation coefficient, we calculate the rank of the data-set. We arrange the ranks according to the numerical value; that is, we give rank 1 to the highest numerical value of the PCA data-set, rank 2 to the second highest, and so on. The Spearman correlation coefficient is the Pearson correlation coefficient of the rank variable of the data-set. Spearman correlation gives information about whether the dependent and independent variables are monotonically increasing or decreasing. For the Kendall correlation coefficient, we find the concordant and discordant pairs. It gives the ordinal association between the variables (Kreyszig *et al.*, 2011; Kendall, 1938).

We choose the smallest value of N from the set of which the PCA data matrix gives us a higher value of Pearson Correlation coefficient compared to the Spearman and Kendall correlation coefficients. Only if the expression of the observable $\xi(z)$ in terms of the polynomial is exact, there would no correlation between the coefficients of the polynomial expression. Our motive is to break the correlation of the coefficient and obtain the polynomial expression of $\xi_{ini}(z)$ as closely as possible to the actual $\xi(z)$. After the reduction of the higher order Principal Component(PC)s, the number of the terms in the polynomial of $\xi_{ini}(z)$ is M . The final functional form of the observable is,

$$\xi_{pca}(z) = \sum_{i=1}^M \kappa_i u_i(z)$$

where, $(u_1(z), u_2(z), \dots, u_M(z))$ and $U = G\mathcal{E}$. After applying PCA, the dimension of the coefficient space $\vec{\kappa}$ is M .

In the earlier work, we have shown that a derived approach where the Principal Component Analysis obtains the observable and then reconstruction of dark energy equation of state parameter is an efficient method to reconstruct dark energy model than directly attempting to reconstruct it. Also, while we can reconstruct the Hubble parameter $h(z)$ very well with PCA, the presence of a differentiation term in the equation given by eqn (3) which relates the EoS with $h(z)$ increases the errors in the reconstruction of $w(z)$.

We address this problem by suggesting a modified approach to bypass the differentiation in calculating EoS from the PCA reconstructed Hubble parameter, distance modulus function, and angular scale of

BAO. This has been done by combining PCA with the Maximum Likelihood Estimation technique (MLE), using Markov Chain Monte Carlo (MCMC) to search for the best fit dark energy model to the PCA reconstructed Hubble parameter, distance modulus, and angular scale. We replace the observational part of the MLE calculation with best-fit curve of $h(z)$, $\mu(z)$, and $\theta_b(z)$ as a function of redshift obtained via PCA. This method omits the dependencies on the number of observational data points. This analysis gives us the machinery to produce the most probable value of the model parameters by constraining the theory with reconstructed PCA data. The errors are the error-functions created from the covariance matrix of PCA data-matrix (Huterer & Starkman, 2003; Sharma *et al.*, 2020; Clarkson & Zunckel, 2010). The error comprises the eigenvalues and eigenfunctions of the covariance matrix (Huterer & Starkman, 2003; Sharma *et al.*, 2020; Clarkson & Zunckel, 2010). The eigenvalues of the covariance matrix quantify the error in the reconstruction of the observable $\xi(z)$. If λ_i are the eigenvalues of the covariance matrix C , then the error associated with each of the components is $\sigma(\alpha_i) = \lambda_i^{1/2}$. For M number of final terms, we have the final error as,

$$\sigma(\xi(z_a)) = \left[\sum_{i=1}^M \sigma^2(\alpha_i) e_i^2(z_a) \right]^{1/2} \quad (10)$$

Eqn(10) gives the error function for a particular reconstructed curve, and we have the error as a function of redshift (Huterer & Starkman, 2003; Clarkson & Zunckel, 2010).

2.2 No-U-Turn sampler

To implement the MCMC search, we use the No-U-Turn sampler (NUTS), which effectively chooses the best parameter region. The No-U-Turn sampler is a modification of the Hamiltonian Monte Carlo (HMC), where the algorithm intrinsically selects the Leapfrog steps (Salvatier *et al.*, 2016; Gelman & Rubin, 1992; Hoffman & Gelman, 2011). The selection of leapfrog steps is crucial in solving the Hamiltonian differential equations of the HMC. At every step, NUTS proceeds by creating a binary tree. In this binary tree, two particles representing progress in the forward and backward directions are created. If these two are represented as $(\mathbf{q}_n^+, \mathbf{p}_n^+)$ and $(\mathbf{q}_n^-, \mathbf{p}_n^-)$ then the NUTS conditions can be given by,

$$\begin{aligned} (\mathbf{q}_n^+ - \mathbf{q}_n^-) \cdot \mathbf{p}_n^- &< 0 \\ (\mathbf{q}_n^+ - \mathbf{q}_n^-) \cdot \mathbf{p}_n^+ &< 0 \end{aligned}$$

In HMC, we move in the phase space of \mathbf{q} and \mathbf{p} in the elliptical path (Gelman & Rubin, 1992; Hoffman & Gelman, 2011). The motivation for introducing the momentum variable \mathbf{p} is to ensure we are exploring the greater area of the parameter space. This is done by moving in an elliptical contour, which we get after solving the dynamical Hamiltonian equation. In NUTS, when we move half of the elliptical path, the sign of the momentum and the position variables are changed, and we stop. This makes the NUTS more efficient than HMC, wherein there is no way to ascertain if we are moving in the region of parameter space that is already explored.

We choose the value of the total sample points M_s by checking the convergence limit using Gelman-Rubin statistic (Salvatier *et al.*, 2016). Gelman-Rubin statistic for convergence is based on the notion that multiple convergence chain appears to be similar to each other; otherwise, they will not converge. It is a standard method to run multiple MCMC chains to test for convergence. Scale reduction factor \hat{r}_o is used to check the Gelman-Rubin convergence. There are two main ways the sequences of MCMC iterations fail to converge. In one case, the chains run in different parts, which have drastic differences in posterior probability densities of the target distribution. On the other, the chains fail to attain convergence. We change the value of M_s until we get $\hat{r}_o = 1$, which is a confirmation of attaining the convergence.

3. Results

We do the analysis described above for the Hubble parameter data, Cepheid Calibrated SNIa data and for the BAO data-set. For the Hubble parameter, we show the results of both the simulated and the real data-set. The simulated data-set is created using the same parameter values as is fixed by (Planck Collaboration *et al.*, 2018). For the simulated Λ CDM data-set we have fixed the values of cosmological parameters as $\Omega_m = 0.3$ and $h_0 = 0.685$. We test the validity of our method and check if the analysis picks up these values. We then apply the method to the real data-set, namely the Cosmic-Chronometer data-set (Moresco *et al.*, 2020; Jimenez *et al.*, 2023; Jiao *et al.*, 2023; Simon *et al.*, 2005; Moresco *et al.*, 2012; Ratsimbazafy *et al.*, 2017; Moresco, 2015) as well as SNIa data-set (Scolnic *et al.*, 2022; Riess *et al.*, 2021; Deng & Wei, 2018; Uddin *et al.*, 2023), then, compare with the usual likelihood analysis results. We also use the transverse BAO data-set from Carvalho *et al.* (2016); Alcaniz *et al.* (2017); Carvalho *et al.* (2020); de Carvalho *et al.* (2018), which consists of 15 transverse BAO measurements (Nunes

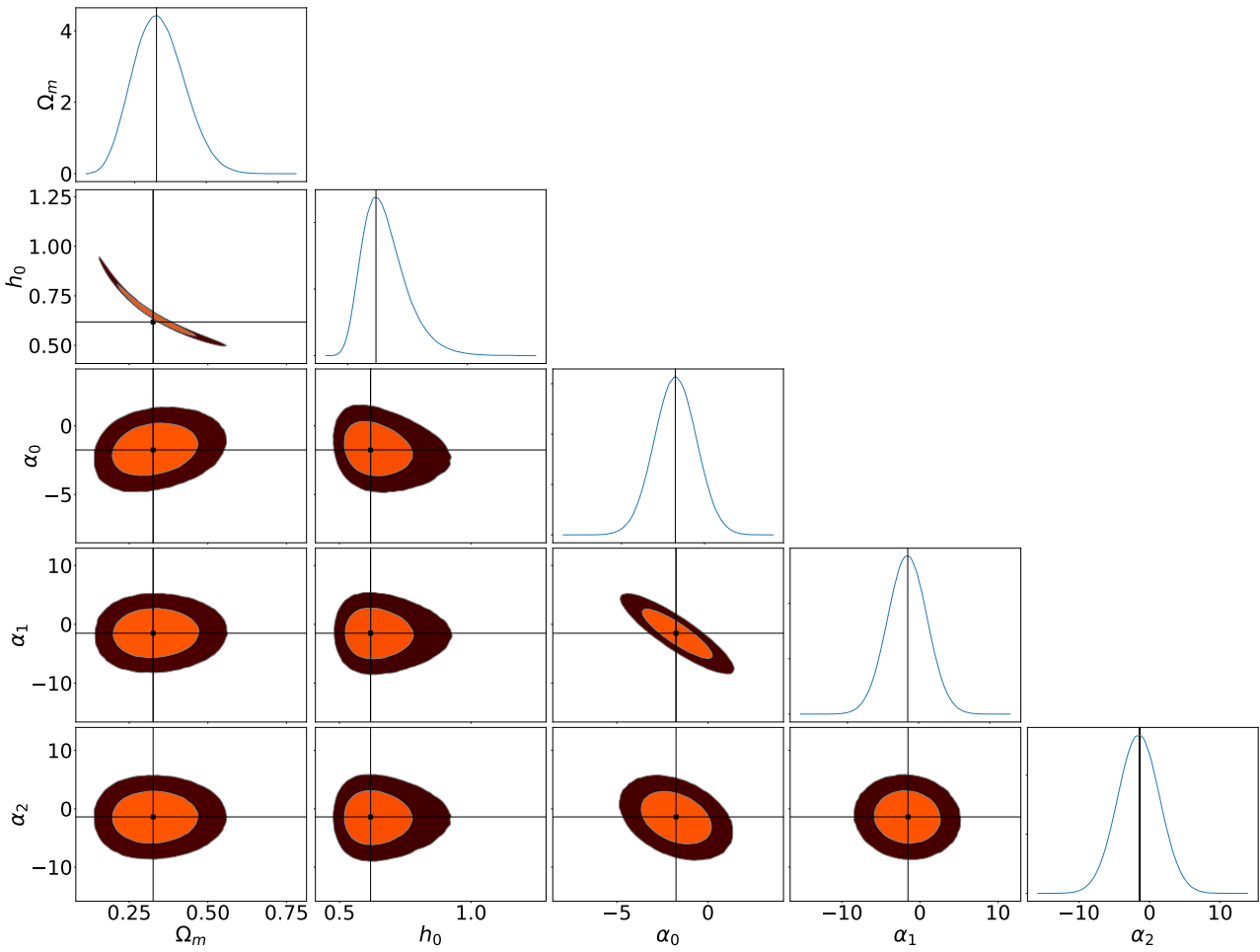


Figure 1: The plot shows the 1σ and 2σ contours for all the parameters along with their marginal probability density plots for the case of the simulated data-set. The first plot of every column is the marginal probability density plot, which give the maximum evidence for the real Hubble parameter data-set.

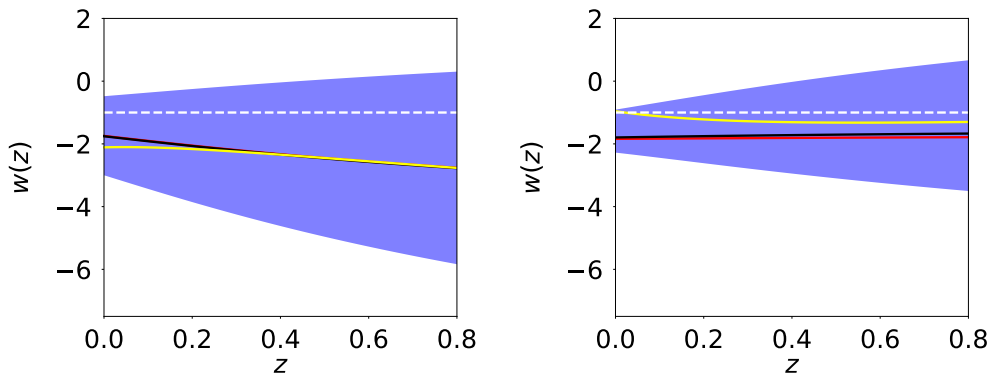


Figure 2: In this figure, we show the 68% confident level range for the equation of state parameter $w(z)$. The figure on the left is for the simulated Hubble parameter data set, and the right is for the real data set. The value of observational points n_d and sample points M_s are 600 and 800000, respectively. The black, red, and yellow curves are the median, mean, and mode of the posterior density function. The cosmological constant model is consistent with the data and is denoted by the dashed line. For both plots, the mean and median lines overlap.

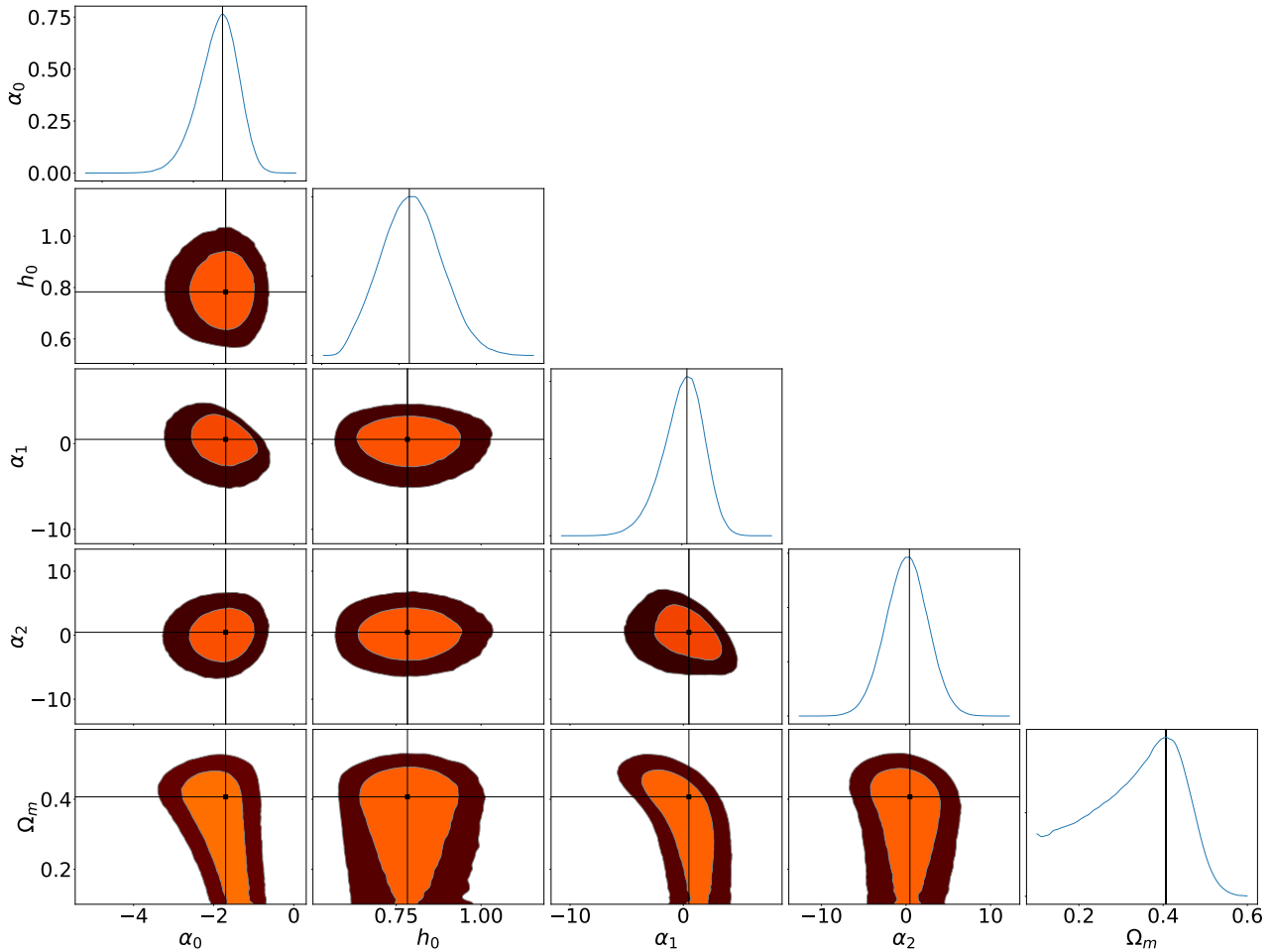


Figure 3: The plot shows the 1σ and 2σ contours for all the parameters along with their marginal probability density plots for the case of real data-set (Zhang *et al.*, 2014; Simon *et al.*, 2005; Moresco *et al.*, 2012; Ratsimbazafy *et al.*, 2017; Moresco, 2015). As in the previous figure, the first plot of every column is the marginal probability density plot.

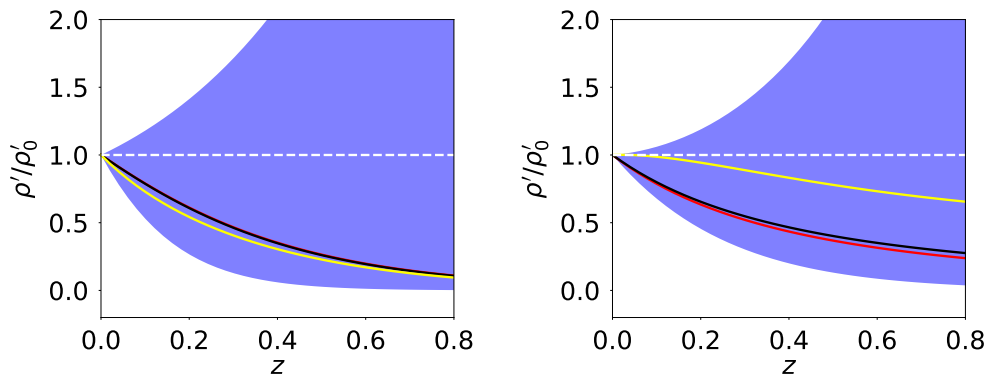


Figure 4: In this figure, we show the 68% confident level range for the dark energy density evolution $\frac{\rho'}{\rho_0}$. Here, ρ' and ρ_0 are the dark energy density at redshift z and at the present time, respectively. Like in figure 2, the left figure is for the simulated Hubble parameter data set, and the right is for the real data-set. The value of observational points n_d and sample points M_s are 600 and 800000, respectively. The black, red, and yellow curves are the median, mean, and mode of the posterior density function. The cosmological constant model is consistent with the data and is denoted by the dashed white line. For both the plots, mean and the median line overlap.

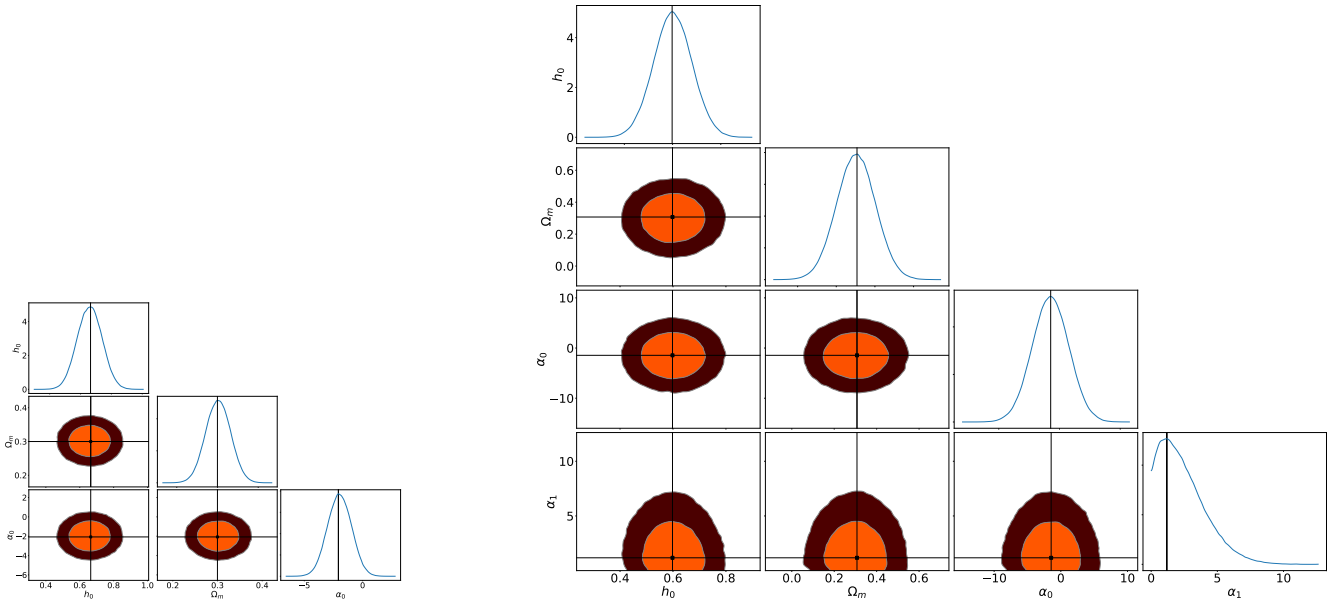


Figure 5: In this figure we show the 1σ and 2σ contours for all the parameters for the w_{CDM} (left) as well as for the w_{CPL} model. Plots in the top and right of the main figures are for the marginal probability density plot for the SNIa data-set. The plots are created for $[n_d, M_s] = [100, 80000]$. Here, we use the Cepheid Calibrated SNIa data-set(Scolnic *et al.*, 2022; Riess *et al.*, 2021; Uddin *et al.*, 2023; Deng & Wei, 2018).

et al., 2020), that are calculated using the public data-releases of the Sloan Digital Sky Survey (SDSS)(York *et al.*, 2000), without assuming a fiducial cosmological model (Carnero *et al.*, 2012; Sánchez *et al.*, 2011).

To get the reconstructed curve of reduced Hubble parameter, distance modulus, as well as angular scale we use $f(z) = \frac{z}{(1+z)}$ as basis variable for simulated as well as observational dataset. This initial basis function gives the best reconstruction as shown in (Sharma *et al.*, 2020). Here, we have the freedom to choose the value of n_d , which is the number of data points in the observed part of MLE. We run the Markov Chain Monte Carlo (MCMC) chain to search for minimum χ^2 , which gives us the likelihood of the PCA dataset. In the MCMC analysis, for Hubble parameter dataset we use normal priors $\mathcal{N}(0.70, 0.2)$ and $\mathcal{N}(0.35, 0.1)$ for reduced Hubble constant h_0 and Ω_m respectively. For the DE parameters, $\vec{\alpha}$ we take $\mathcal{N}(0, 3)$. Here, $\mathcal{N}(x_{mean}, x_{mode})$ represents the normal probability density function with mean x_{mean} and spread of x_{mode} . For Cepheid Calibrated SNIa data, we use the data archive given in Riess *et al.* (2021); Uddin *et al.* (2023); Deng & Wei (2018). In the MLE part, we take half normal with a standard deviation of 0.4 as a prior of Ω_m and for $\vec{\alpha}$ we take $\mathcal{N}(-2, 1.5)$. In the case of the BAO data-set, we use the same priors as for Hubble parameter dataset.

We choose the largest possible value for n_d , which is limited by the computing power. We then check the results for different values of n_d and M_s . Moreover, we find out the posterior distribution’s mean, median, and

mode. For $m = 3$ in eqn(2), we do the analysis for different values of n_d and M_s . $m = 3$ is the CPL parameterization along with the next order term (Chevallier & Polarski, 2001; Linder, 2003). We vary n_d in the range 100 to 800 whereas M_s in the range 1000 to 800000 and find out mean, median, and mode as well as 1σ and 2σ ranges of $\omega_m, h_0, \vec{\alpha}$.

From the mode plot of the posterior of the model likelihood of fig(2) and fig(4), we can see the difference between the old cosmic chronometer data-set (Zhang *et al.* (2014); Simon *et al.* (2005); Moresco *et al.* (2012); Ratsimbazafy *et al.* (2017); Moresco (2015)) with the new cosmic chronometer data-set(Moresco *et al.* (2020); Jimenez *et al.* (2023); Jiao *et al.* (2023)). For the particular cosmological model of eqn(2), with the NUTS algorithm, PCA reconstruction brings $w(z)$ closer to the $w(z) = -1$ in comparison to the old cosmic chronometer data-set.

In Figures 3 and 1, we show results for $n_d = 600$, where we fix the number of sample points at $M_s = 80,000$. This particular choice of n_d and M_s gives us the closest approximation of the model parameters for the simulated Hubble parameter data. Also, we see that about this value of n_d and M_s we get the smallest variation in 1σ and 2σ ranges of the model parameters, with the variation of these two quantities. In particular for $(n_d, M_s) = (600, 800000)$ & $(1000, 50000)$ the difference in 1σ and 2σ ranges are of the order of $O(-1)$ for $\vec{\alpha}$ and $O(-2)$ or less for Ω_m and h_0 . For the Hubble parameter data-set, the mean of the posterior of h_0 and

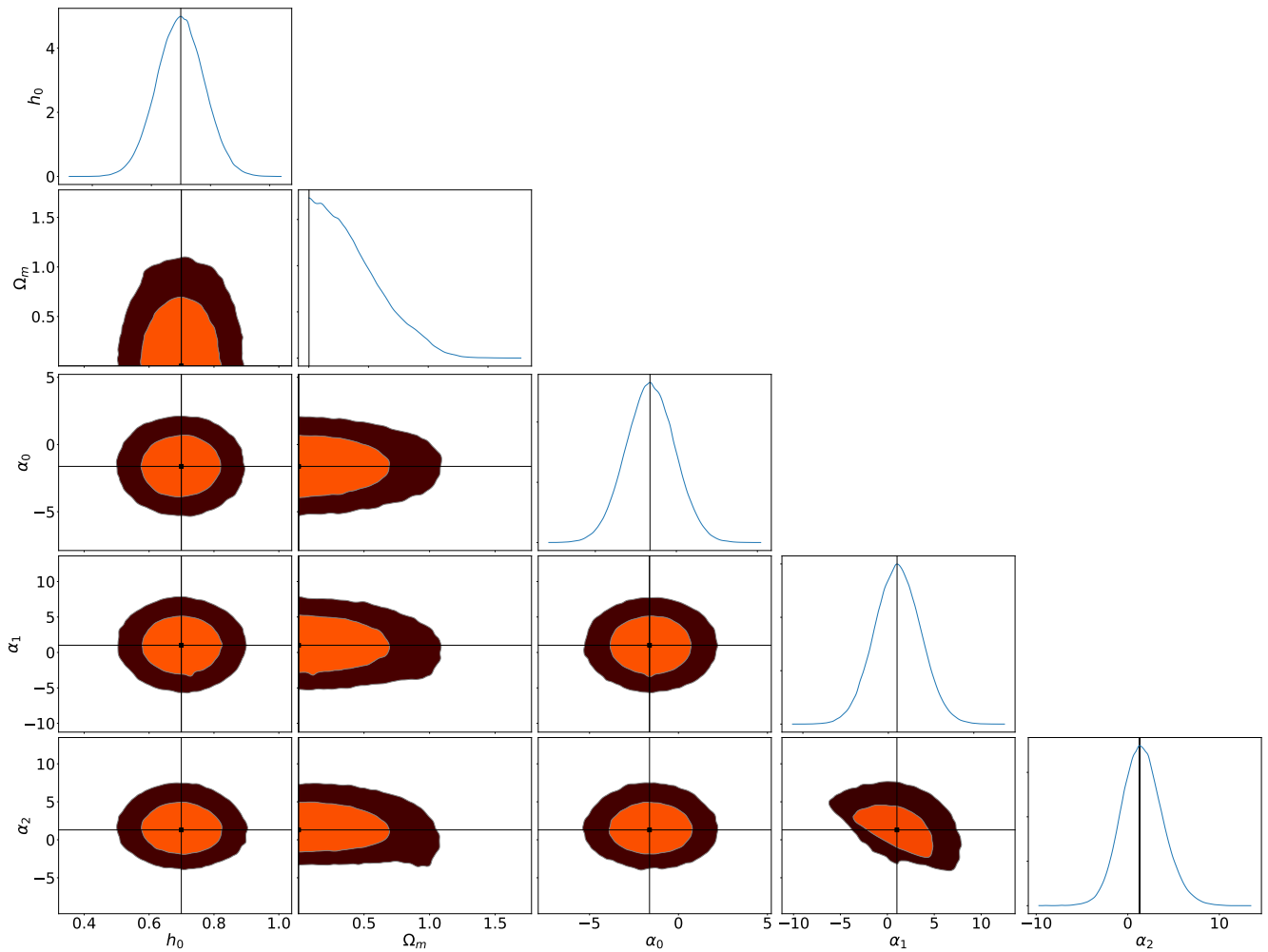


Figure 6: The plot shows the 1σ and 2σ contours for all the parameters along with their marginal probability density plots for the case of distance modulus data-set (Scolnic *et al.*, 2022; Riess *et al.*, 2021; Uddin *et al.*, 2023; Deng & Wei, 2018). For the plot we consider $[n_d, M_s] = [100, 80000]$. The models considered here is the model described in eqn(1, 2). Plots in the top and right of the main figures are for the marginal probability density plot for the SNIa data-set.

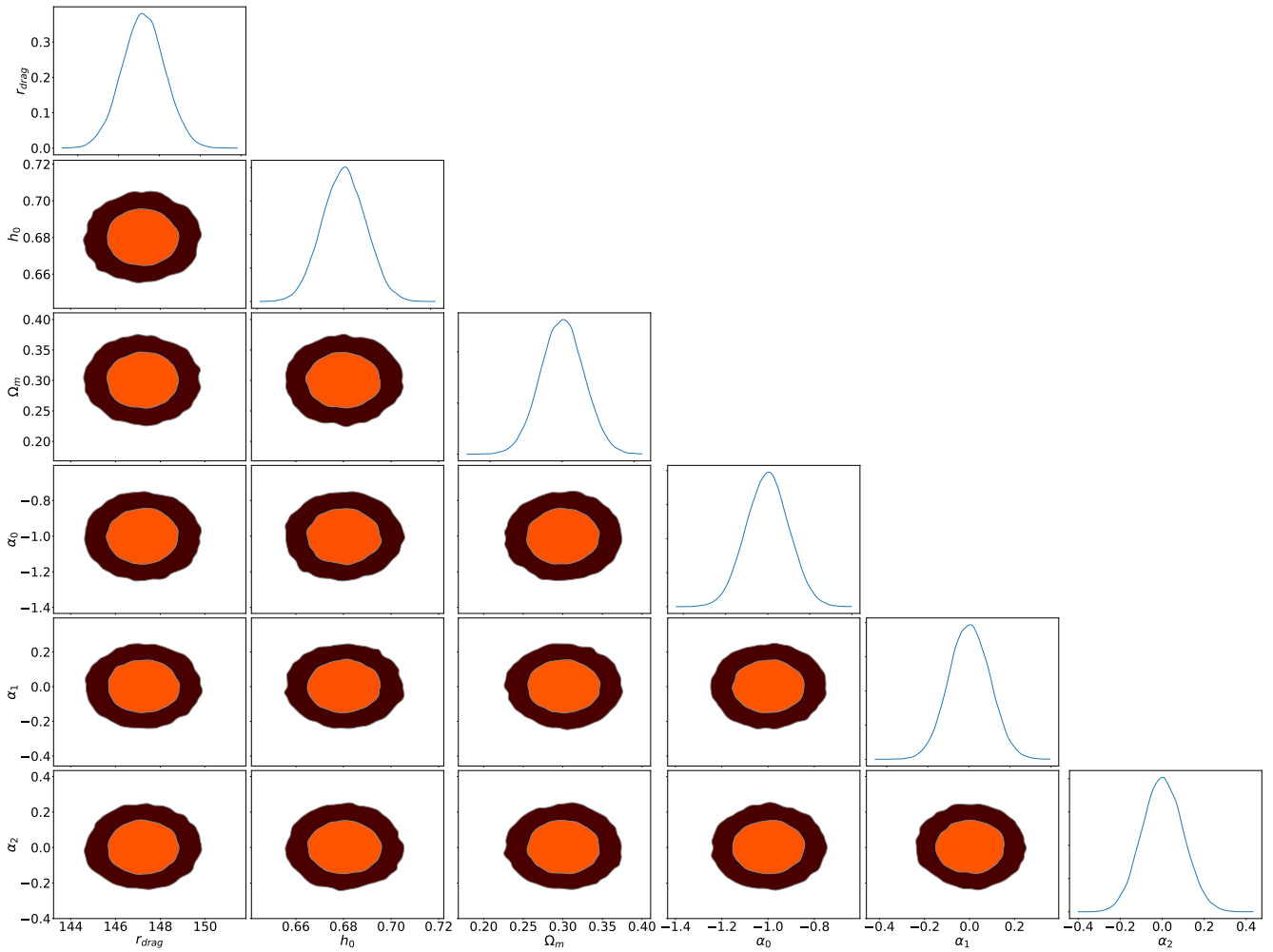


Figure 7: The plot shows the 1σ and 2σ contours for all the cosmological parameters along with r_{drag} . Their marginal probability density plots for the case of transverse BAO data-set (Scolnic *et al.*, 2022; Riess *et al.*, 2021; Uddin *et al.*, 2023; Deng & Wei, 2018) are shown in the first subplot of each column. For the plot we consider $[n_d, M_s] = [50, 10000]$. The models considered here is the model described in eqn(1, 2).

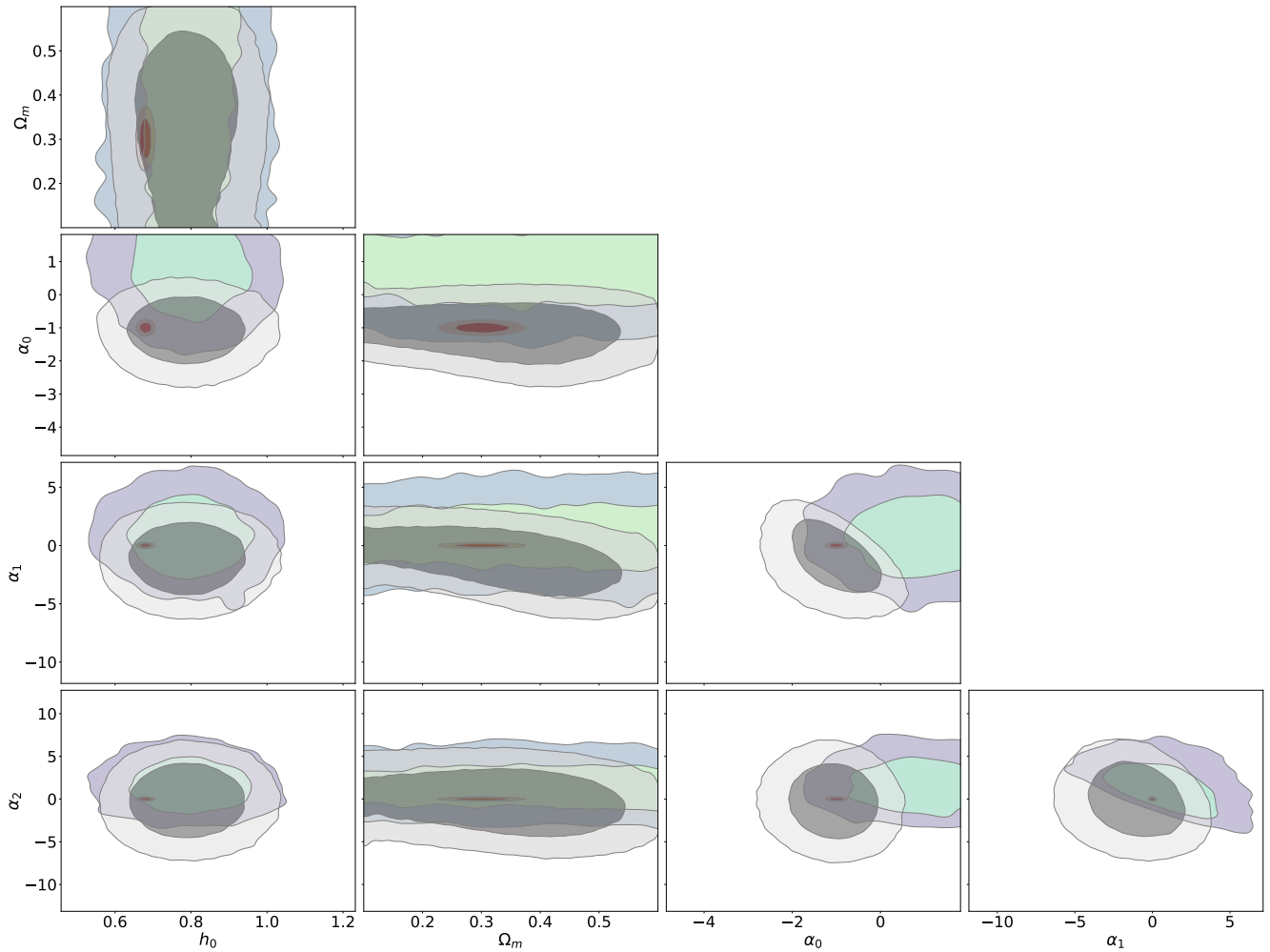


Figure 8: The plot shows the joint likelihood assumed by all the data-sets. The 1σ and 2σ contours for Hubble parameters are shown in green-blue colors respectively, while the same for the SNIa are in grey colors, and for the BAO it is in red. The model considered here is the model described in eqn(1, 2). Here, for all the data-set we run the chains for $(n_d, M_s) = (50, 10000)$

data-type and model	parameter	1σ	2σ	best-fit
Hz Simu (w_{model})	h_0	[0.55, 0.7161]	[0.496, 0.847]	0.674
	Ω_m	[0.238, 0.415]	[0.169, 0.508]	0.328
	α_0	[-3.01, -0.48]	[-4.24, 0.739]	-1.74
	α_1	[-4.379, 1.145]	[-7.047, 3.85]	1.602
	α_2	[-4.501, 1.394]	[-7.314, 4.3]	-1.54
Hz Real (w_{model})	h_0	[0.689, 0.885]	[0.601, 0.974]	0.784
	Ω_m	[0.247, 0.473]	[0.107, 0.488]	0.328
	α_0	[-2.278, -0.998]	[-2.94, -0.83]	-1.84
	α_1	[-4.492, 1.023]	[-7.143, 3.75]	0.08
	α_2	[-1.59, 2.296]	[-5.33, 5.422]	0.09
SNIa (w_{CDM})	h_0	[0.579, 0.739]	[0.503, 0.815]	0.703
	Ω_m	[0.272, 0.332]	[0.242, 0.361]	0.345
	α_0	[-3.01, -0.965]	[-3.98, -0.019]	-1.89
SNIa (w_{CPL})	h_0	[0.52, 0.68]	[0.45, 0.76]	0.645
	Ω_m	[0.201, 0.401]	[0.105, 0.498]	0.301
	α_0	[-4.49, -0.151]	[-7.40, 4.36]	-1.47
	α_1	[0.0072, 3.02]	[$\mathcal{O}(-5)$, 5.78]	2.44
SNIa (w_{model})	h_0	[0.618, 0.777]	[0.542, 0.855]	0.696
	Ω_m	[$\mathcal{O}(-5)$, 0.46]	[$\mathcal{O}(-5)$, 0.894]	0.329
	α_0	[-3.12, -0.122]	[-4.56, 1.36]	-1.58
	α_1	[-1.65, 3.7]	[-4.24, 6.33]	0.957
	α_2	[-0.809, 3.62]	[-2.81, 6.174]	1.43
BAO (w_{model})	h_0	[0.67, 0.69]	[0.66, 0.699]	0.68
	Ω_m	[0.269, 0.328]	[0.241, 0.351]	0.30
	α_0	[-1.10, -0.903]	[-1.2, -0.81]	-1.0
	α_1	[-0.092, 0.104]	[-0.192, 0.19]	0.0
	α_2	[-0.099, 0.096]	[-0.19, 0.196]	0.01

Table 1: This table gives the 1σ and 2σ ranges for parameters, h_0 , Ω_m and $\vec{\alpha}$, for all the different model and the data-type for which we run our complete analysis. For the cosmic chronometer data-set we use both the simulated and the real data-sets and apply it to w_{model} . For SNIa data we do our analysis for w_{CDM} , w_{CPL} as well as the dark energy model of eqn(2) with $m = 3$. Here $\vec{\alpha}$ are the parameters of dark energy equation of state parameter. The last column of the table corresponds to the best-fit value of the parameter of the model given the data-set.

Ω_m from the algorithm are $h_0 = 0.68$ and $\Omega_m = 0.34$, which are very close to the assumed values to produce the simulated data-set, $h_0 = 0.685$ and $\Omega_m = 0.3$. In table 1 we show the 1σ and 2σ ranges for the parameters, along with their best-fit values. The mean of the posterior of h_0 and Ω_m for the real Hubble parameter data are $h_0 = 0.71$ and $\Omega_m = 0.35$, respectively. Also, we present our results for SNIa data-set (Scolnic *et al.*, 2022; Riess *et al.*, 2021; Uddin *et al.*, 2023; Deng & Wei, 2018) as well as BAO data-set (Carvalho *et al.*, 2016; Alcaniz *et al.*, 2017; Carvalho *et al.*, 2020; de Carvalho *et al.*, 2018; Nunes *et al.*, 2020). For SNIa data-set, we show our results for w_{CDM} and w_{CPL} in the fig(5). For the model of eqn(2) with $m = 3$, we show our results in fig(6). We present our results for $(n_d, M_s) = (100, 80000)$ for the SNIa data-set. Table(1) gives a comparison; this table can be extended to different data-sets and models.

In fig(7), we present results for the BAO data-set, using the DE model with $m = 3$ of eqn(2). We see, both from the fig(7), and the combined joint analysis plot fig(8) that BAO gives tighter constraints in comparison to Hubble parameter and SNIa data-sets. For fig(8) and fig(7) we use $(n_d, M_s) = (50, 10000)$, and this choice is done under the available computational power. From the fig(7) we can see that PCA + MCMC gives very good reconstruction even with a small number of sample points M_s . The 1σ range of r_{drag} from our method is [146.1, 148.2].

It is also evident from the fig(2, 3, 4, 5, 6, 7) that $w(z) = -1$ is well within the 1σ range of $w(z)$ parameters($\vec{\alpha}$). The plot of $w(z)$ and $\rho(z)/\rho_0$ are similar for both real and simulated data-set. The difference in $w(z)$ and $\rho(z)/\rho_0$ curve between simulated and real Hubble parameter data are 0.445 and 0.026, respectively. Here, $\rho(z)$ and ρ_0 are the total energy density at redshift z and at present. The dark energy density plot, $\rho'(z)/\rho'_0$ vs. z , for simulated and real Hubble parameter data-set are also similar, and the maximum difference between them for Hubble parameter data-set is 0.31.

We restrict to the $m = 3$ cut-off in eqn(2) for $(n_d, M_s) = (600, 800000)$, largely due to the computational power available to us at present. In the table 2, for $(n_d, M_s) = (100, 100)$ we use the algorithm upto $m = 10$. We find out that for the Hubble parameter data-set the better constraint on the parameter space for $m \geq 4$ needs to be done with $(n_d, M_s) \geq (600, 800000)$. In a follow-up work we are trying to optimize the algorithm to constrain the parameter space with large enough values of m , and draw the physical conclusion over it. The parametrization of $w(z)$ and $\frac{\rho'_{de}}{\rho'_0}$ have the same physical implication, which is shown in fig(2, 4). The dark energy density can be derived analytically for these parameterizations, and fixing the dark energy

equation of state parameter determines the evolution of the energy density as a function of time.

In the MCMC run for both the real and simulated Hubble parameter data-set, with $(n_d, M_s) = (600, 800000)$, the value of Gelman-Rubin convergence factor \hat{r}_o is 1. For SNIa MCMC run $(n_d, M_s) = (100, 80000)$ gives the value of $\hat{r}_o = 1$. To check the convergence, we not only check the \hat{r}_o factor and eliminate those iterations which do not satisfy the $\hat{r}_o \approx 1$ criteria, but we also check the trace plots, rank bar plots and the rank vertical line plots of the posterior sampling for visual confirmations (Gelman & Rubin, 1992; Brooks & Gelman, 1998; Cowles & Carlin, 1996).

The error bars of the parameters, in table (1), are derived when error function from PCA is considered. Hence the 1σ , 2σ ranges are affected by the error functions we introduce in the MLE. For w_{cpl} , with the Pantheon data-set, when we consider a half-Normal probability distribution for the error part of the MLE, the range of h_0 changes to [0.6005, 0.6584], which is almost three times smaller than the range when PCA error function is considered. PCA error function is created solely from the data structure we provide in the first step of PCA. With the improvement of error-bars in the original data-points the range of the parameters will reduce significantly.

We also analyze with the classical Metropolis-Hastings (MH) as well as the Hamiltonian Monte Carlo sampler (HMC). For comparison with MH and HMC, we do the analysis with $(n_d, M_s) = (600, 800000)$ and $(n_d, M_s) = (100, 80000)$ for Hubble parameter and Supernovae data respectively. Our analysis shows that NUTS and Hamiltonian Monte Carlo sampler (HMC) perform better than Metropolis-Hastings sampler (MH). For more than six continuous parameters and with the same CPU power, NUTS improves speed by a factor of 2.4 to complete the analysis. Details of the time taken by the MH and NUTS are given in Appendix B. The plots for the real Hubble parameter data-set, with the MH is shown in Appendix B. Again, NUTS is better than HMC as after picking up the leapfrog steps, NUTS stops automatically when the NUTS conditions are satisfied. It has been explicitly shown in (Hoffman & Gelman, 2011) that the NUTS algorithm is more efficient. Convergence plots for the NUTS sampler in the case of the Hubble parameter data-set are shown in the Appendix A. and that of the MH is shown in Appendix B..

4. A comparison with other methods

The reconstruction of $H(z)$, $\mu(z)$ and $\theta_b(z)$ from the PCA algorithm, which is described in the sec(2.) and

in Sharma *et al.* (2020) is qualitatively different from the other PCA techniques employed in the literature Huterer & Starkman (2003); Clarkson & Zunckel (2010); Huterer & Cooray (2005); Zheng & Li (2017); Ishida & de Souza (2011). The starting assumption is that the function $h(z)$, $\mu(z)$ and θ_b are smoothly varying over redshift z . This is a reasonable choice as described by the current data-sets, (Moresco *et al.*, 2020; Jimenez *et al.*, 2023; Jiao *et al.*, 2023; Simon *et al.*, 2005; Moresco *et al.*, 2012; Ratsimbazafy *et al.*, 2017; Moresco, 2015; Scolnic *et al.*, 2022; Riess *et al.*, 2021; Deng & Wei, 2018; Uddin *et al.*, 2023; Carvalho *et al.*, 2016; Alcaniz *et al.*, 2017; Carvalho *et al.*, 2020; de Carvalho *et al.*, 2018). Different variants of PCA techniques have been adopted in Liu *et al.* (2019) and Liu *et al.* (2016). Before creating a different set of simulated Hubble data to construct the covariance matrix Liu *et al.* (2019) uses an error model. While Liu *et al.* (2016) use the weighted least square method and combine it with PCA.

We apply MLE to the observed data-sets with the reconstruction functional form of PCA. Including a Cosmological model is only in the final part of our methodology, where we use the MLE technique. MCMC chain with the NUTS, over the model-independent reconstruction of PCA gives unbiased constraints on the model parameters. Fisher matrix computation is one of the major ways to PCA reconstruction (Nesseris & García-Bellido, 2013; Huterer & Starkman, 2003; Clarkson & Zunckel, 2010; Huterer & Cooray, 2005; Zheng & Li, 2017; Ishida & de Souza, 2011; Crittenden *et al.*, 2009; Miranda & Dvorkin, 2018; Hart & Chluba, 2019; Hojjati *et al.*, 2012; Nair & Jhingan, 2013; Hart & Chluba, 2022b). Our methodology calculates the Covariance matrix, which quantifies the correlation and uncertainties directly from the PCA data matrix described in the section 2.. Reduction of dimension, which is a distinctive feature of the PCA reconstruction, omits the noise part from the PCA data matrix. Therefore, the parameter constraints that are done by replacing the observational part with the PCA reconstructed part will constrain the parameter in a more reasonable way. One important feature of the (PCA + MCMC) methodology is that it will also work for sparse data sets. In comparison to the classical techniques, it can be easily generalized to a higher dimension of parameter space with little expense of computational time, as described in sec(2.) and showed quantitatively in 5..

5. Conclusions

In this paper, we combine the Principal Component Analysis reconstruction with the Markov Chain Monte Carlo tool to determine cosmological parameters. We assume the Taylor series expansion of the equation of state parameter in terms of the scale factor as the parameterization of the dark energy equation of state. When the method of PCA, along with correlation coefficient calculation is combined with the MCMC tool, we have the freedom of selecting the number of points in the observational part of maximum likelihood method. We use the No-U-Turn Sampler for this analysis.

We first test the method on simulated data and check if the values assumed for the cosmological parameters are reconstructed effectively. We see that the predictions for the model parameters are consistent with the assumed values. The parameter estimation does not depend strongly on the prior probability assumption, and the idea can be generalized to other data-sets as well as different sampling techniques. The relation between the Hubble parameter and the equation of state of dark energy also contains the first differentiation of the Hubble parameter, which introduces an unwanted error in the equation of state predictions. Similarly, for SNIa and BAO data-sets the relation between the distance modulus as well as the angular scale with the EoS of dark energy contains first and second order differentiation.

The present method eliminates the error that arises from the first and higher order differentiation of the observable to infer the value and ranges of the Equation of State of dark energy. In this work, we only use the error function that comes directly from the PCA algorithm, and one can use different error functions in the error part of the MLE as well. It is clear from the results that, for the simple model of dark energy we take, the allowed range of cosmological parameters is consistent with other analyses, and the cosmological constant model is well within the allowed range of models for both the Hubble parameter and distance modulus dataset. This analysis can be extended to other dark energy models. Here the advantage is that the complete functional form of the observable of the dataset is obtained; in the present work, the Hubble parameter and distance modulus as a function of redshift are determined. The second step is deriving the dark energy equation of state parameter. The method is suitable for different types of data and merits future analysis. It depends only on the model-independent reconstruction of the data-set and the error associated with it. Improvement of even a single data-point leads to an increase of the constraining power of our method. With the upcoming improved

Hubble parameter, SNIa and BAO data-sets, the application of the method will lead to better constraints and a much easier distinction between different dark energy models. Also, the method discussed here can be used as a model selection tool in those data-sets with fewer data-points.

Appendix A. Checks for convergence

Here, we show the trace-plot, rank bar plots and vertical line plots for the NUTS in the case of both simulated and real Hubble parameter data-sets. These plots are essential to check the convergence of the sample as well as the efficiency of the sampler.

As introduced in Vehtari *et al.* (2019), rank plots are histograms of the rank posterior draws, plotted separately for each chain. In our case all the four chains are targeting the same posterior, hence we expect the ranks in each chain to be uniform. The similar rank plots of fig(10) and fig(13) indicates good mixing of the chains.

To assess the MCMC methods we have to measure how good the MCMC estimates are, which could be done using autocorrelation time, the variance of the estimate, or the effective sample size. The autocorrelation of a variable measures the relationship between its present value with any of the past value which we can access. If instead of one value we compare the current series of values with the past historical data it is called autocorrelation time series. Fig(11) and fig(14) gives the autocorrelation for all the four chains. The classical sample techniques like Metropolis-Hasting or Hamiltonian Monte Carlo create autocorrelated samples if the number of continuous parameters are very large. NUTS works very effectively in the case of parameter space which consists of large number of continuous variables (Salvatier *et al.*, 2016; Gelman & Rubin, 1992; Hoffman & Gelman, 2011).

Fig 9, 10, and 11 shows the convergence of the MCMC chains for the simulated Hubble parameter data-set. These plots are created for $(n_d, M_s) = (600, 800000)$. The convergence and the ability to draw successful samples from the parameter space is apparent for $(n_d, M_s) = (600, 800000)$ set in the case of Hubble parameter data-set. The same application for the real Hubble parameter data is shown in fig 12, 13, and 14. Fig(11, 14) gives the auto-correlation of different parameters for different MCMC chains. We see from fig(11, 14) that auto-correlation of the parameters for different chains are zero. For SNIa data-set also, the

auto-correlation as well as the trace and rank-bar plots are similar, and shows the convergence of the MCMC chain.

Appendix B. Convergence plots for Metropolis-Hasting

For the comparison purpose we here give the trace-plot, rank-bar plot and vertical along with the contour plots for the real Hubble parameter data-set using Metropolis-Hasting algorithm (MH) fig(15,16, 17, 18). The number of data-points as well as the the sample points are same as in the NUTS algorithm. Markov chains are run for the simulated data-set. As we can see from the maximum evidence plots in the left of these figures, the convergence of the four chains along with their overlap is much less efficient than in the case of NUTS algorithm. The the marginal posteriors of each stochastic random variables of the parameter space shows the same lack of convergence for the real data-set using MH. Convergence plot for the simulated data-set are also similar. For all the convergence plots the value of simulated data-set and the sample points for the MCMC chains are same as in the case of NUTS algorithm, $(n_d, M_s) = (600, 800000)$. Figure 15 shows that for fix computational power and with the same values of (n_d, M_s) , NUTS constrains the parameter space in a better way than the MH.

To compare the time taken by both NUTS and MH, we run the four chains of MCMC with model of eqn(1,2) and the real Hubble parameter data-set. For different number of parameters we run the MCMC chains of MH and NUTS with a 64 bit x86_64 architecture computer. The results are given in the table 2. We see that when the number of continuous parameter increases NUTS takes much smaller time then the traditional MH algorithm. We run the program with $(n_d, M_s) = (100, 100)$. These time periods are calculated as an average over the 20 identical runs.

When the number of continuous parameters increases NUTS works in a better way in comparison to MH. The fig(15,16, 17, 18) are clear indication to this. NUTS exploits the gradient information of the parameter space to achieve the must faster convergence in comparison to the MH. This can be clearly seen for the models with larger continuous parameter. Salvatier *et al.* (2016); Gelman & Rubin (1992); Hoffman & Gelman (2011) provide a clear theoretical basis on which the effectiveness of the NUTS can be put above the MH.

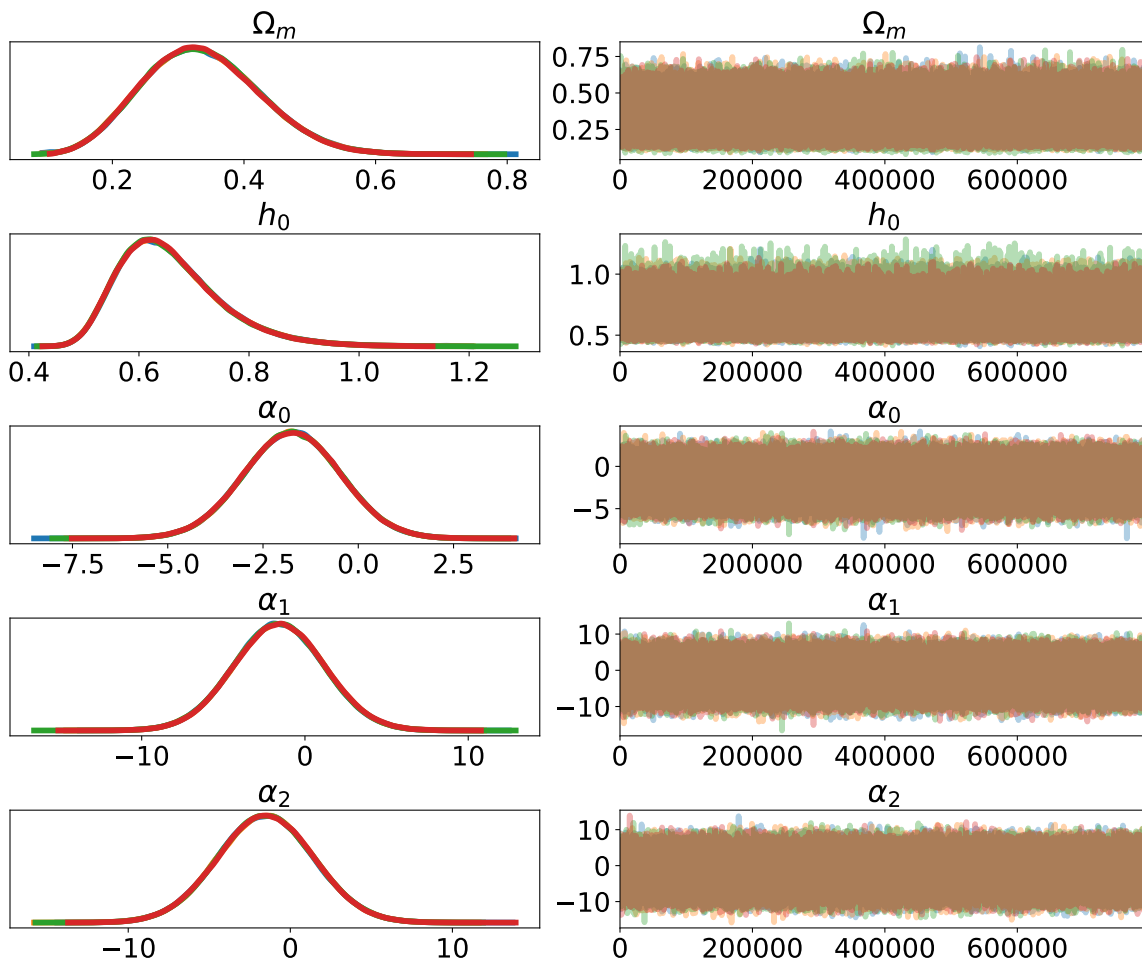


Figure 9: The column on the left consists of a smoothed histogram, using kernel density estimation of the marginal posteriors of each stochastic random variable. From top to bottom, the random variables are density parameters for matter Ω_m , reduced Hubble constant h_0 , and the parameters of the equation of state of dark energy α_i . The right column contains the samples of the Markov chain plotted in sequential order. There are four MCMC chains that are plotted in different colors. These plots are created with $(n_d, M_s) = (600, 800000)$ and all are for simulated Hubble parameter data-set. We use the same values of n_d and M_s in subsequent plots.

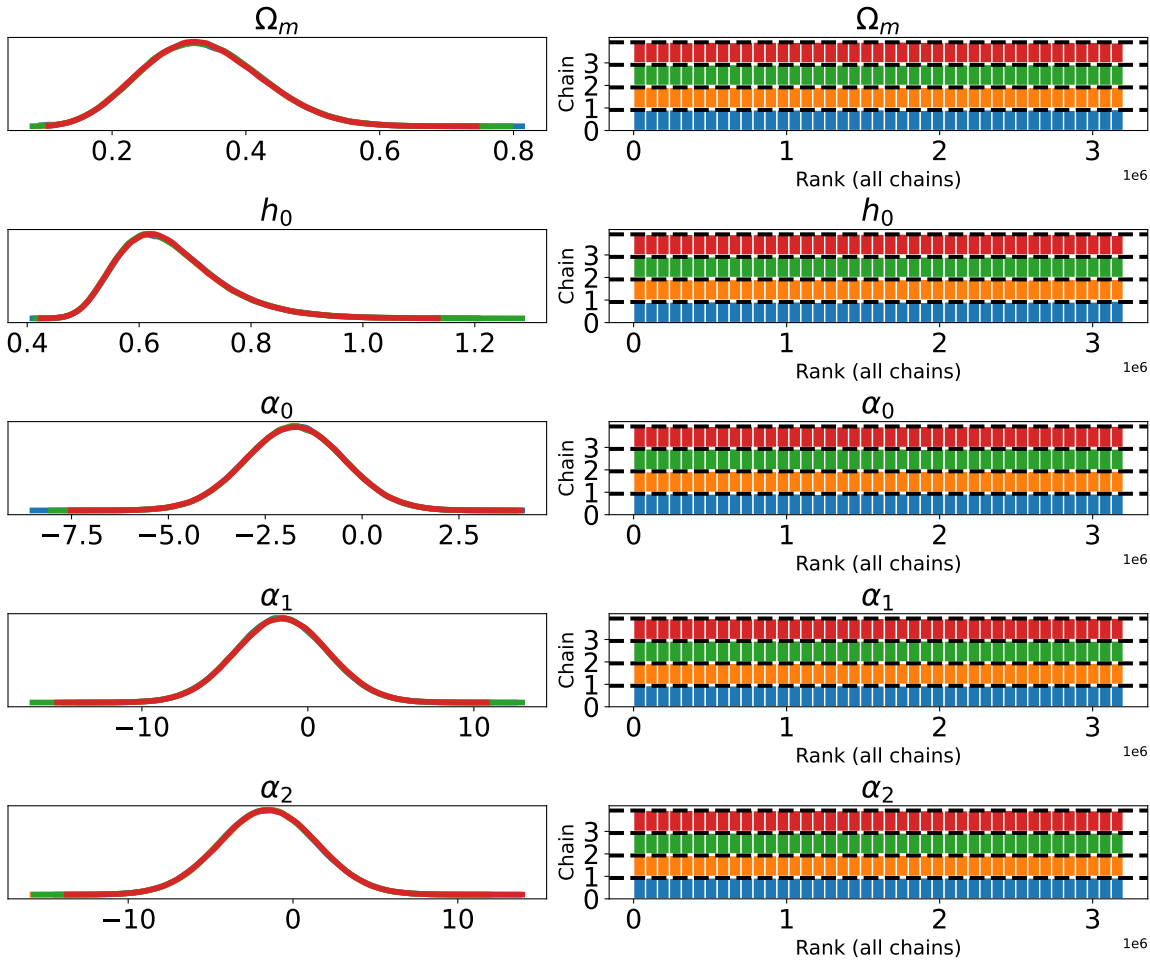


Figure 10: Smoothed histogram using kernel density estimation of the marginal posteriors of each stochastic random variable. From the top to bottom, the random variables are density parameters for matter Ω_m , reduced Hubble constant h_0 , and the parameters of the equation of state of dark energy α_i . The right column shows the number of successful draws from the parameter space, which depends upon the sample size chosen as well as the prior theory. The four MCMC chains are plotted in different colors and all are independent of each other.

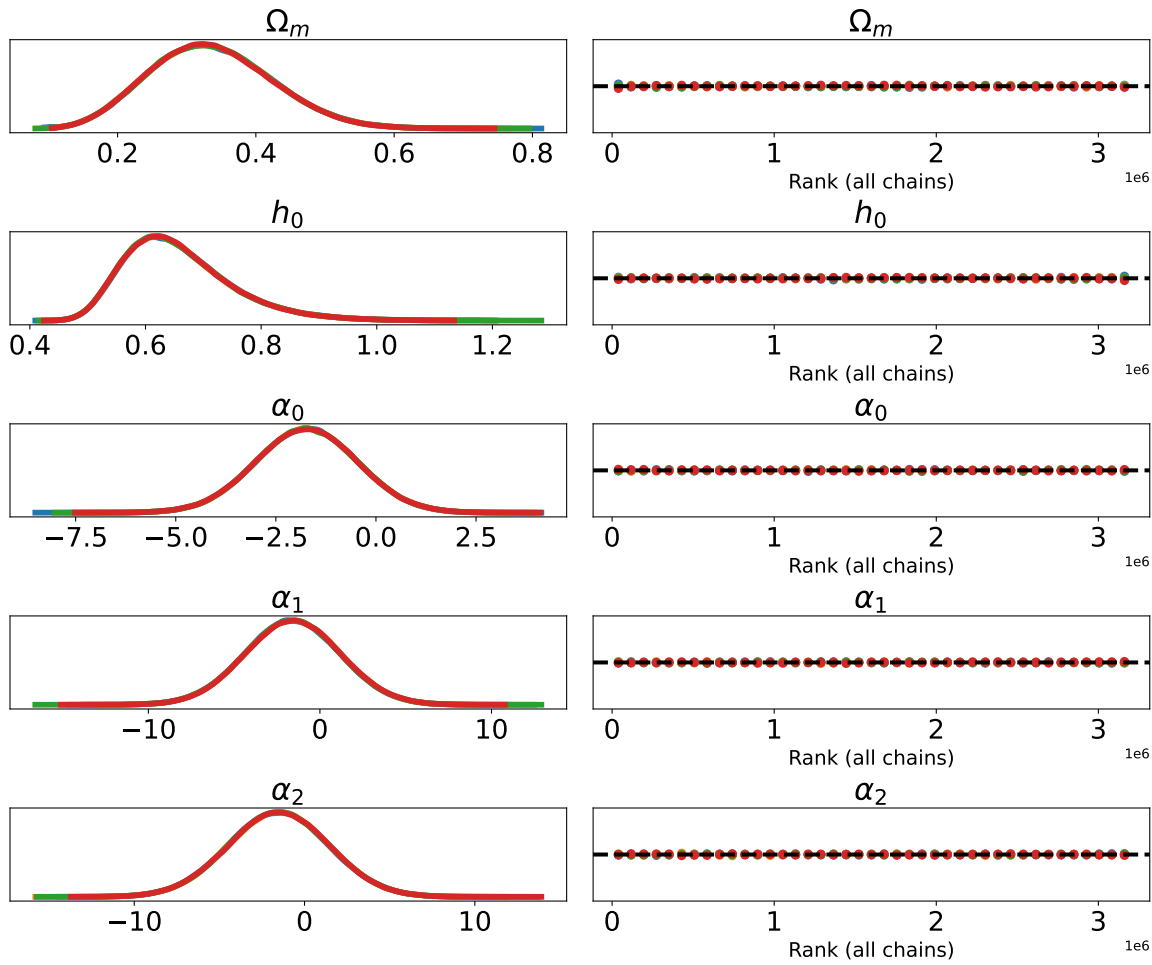


Figure 11: In this figure, the left column consists of a smoothed histogram, using kernel density estimation of the marginal posteriors of each stochastic random variable. The right-hand column gives the auto-correlation for all the random variables for all four independent chains, which are depicted with vertical lines.

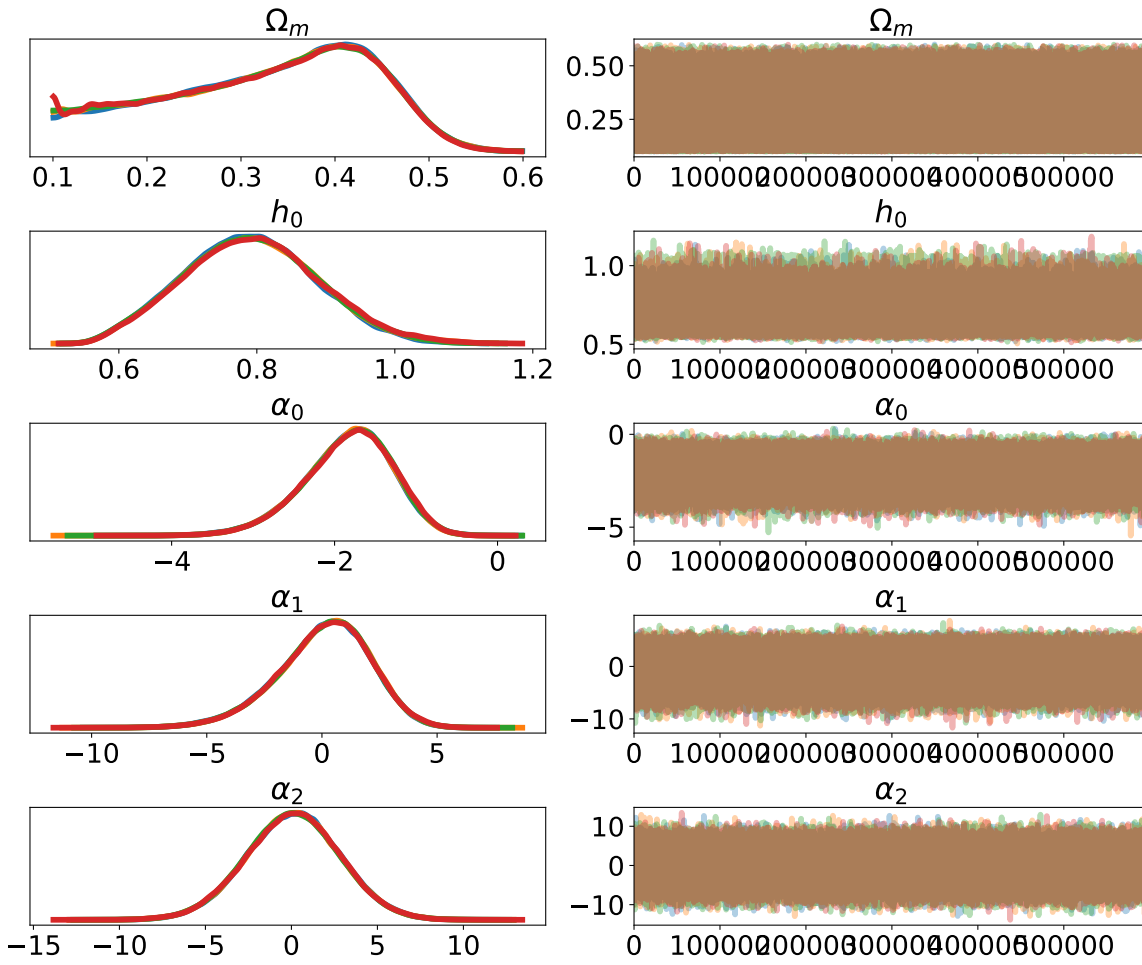


Figure 12: In this figure, the left column consists of a smoothed histogram, using kernel density estimation of the marginal posteriors of each stochastic random variable. The parameters are same as those in fig(9). The right column contains the samples of the Markov chain plotted in sequential order. These plots are also created with $(n_d, M_s) = (600, 800000)$ and all the plots are for observed Hubble parameter data-set.

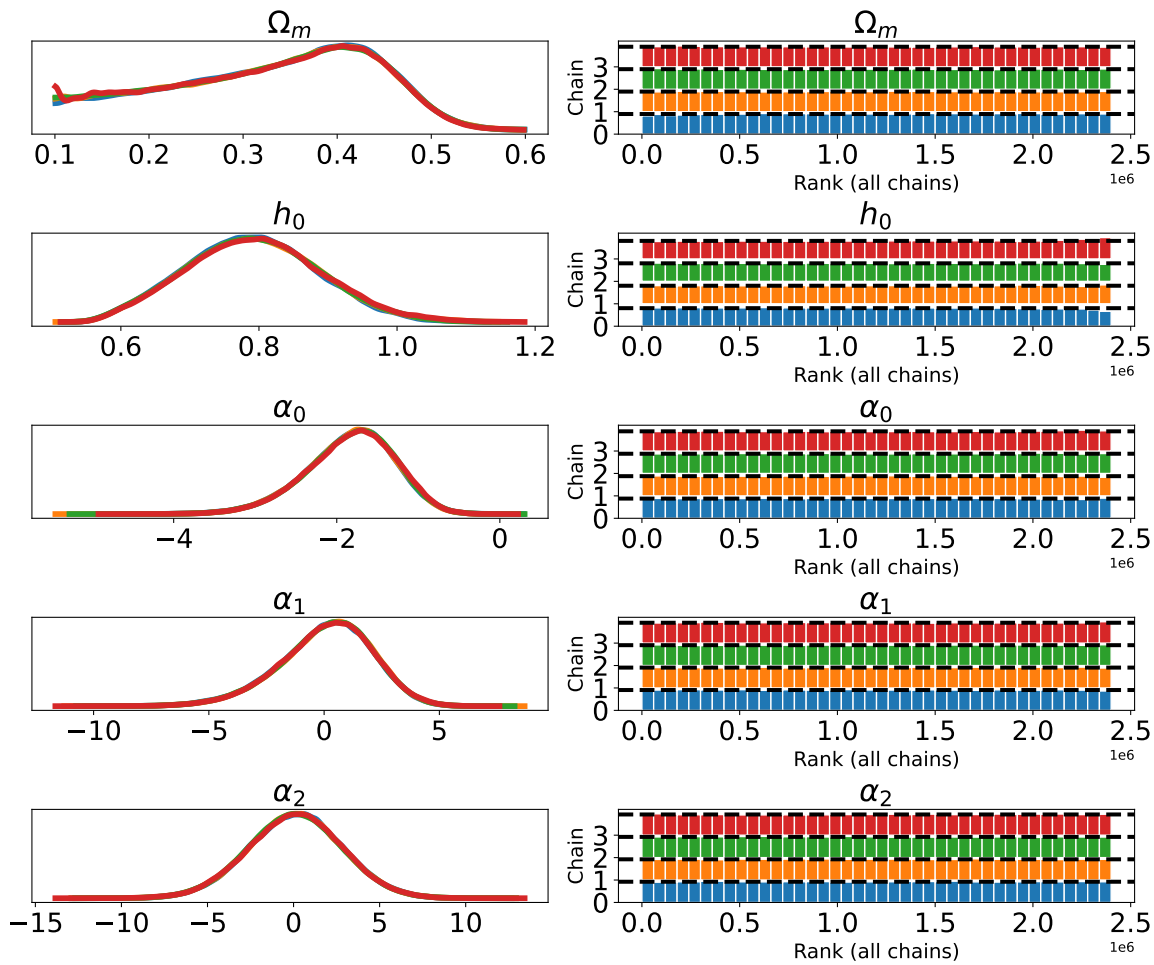


Figure 13: The random variables plotted here are the same as in the previous figures and in the same order. The right column shows the number of successful draws from the parameter space, which depends upon the sample size chosen as well as the prior theory. The four MCMC chains are plotted in different colors and all the chains are independent of each other.

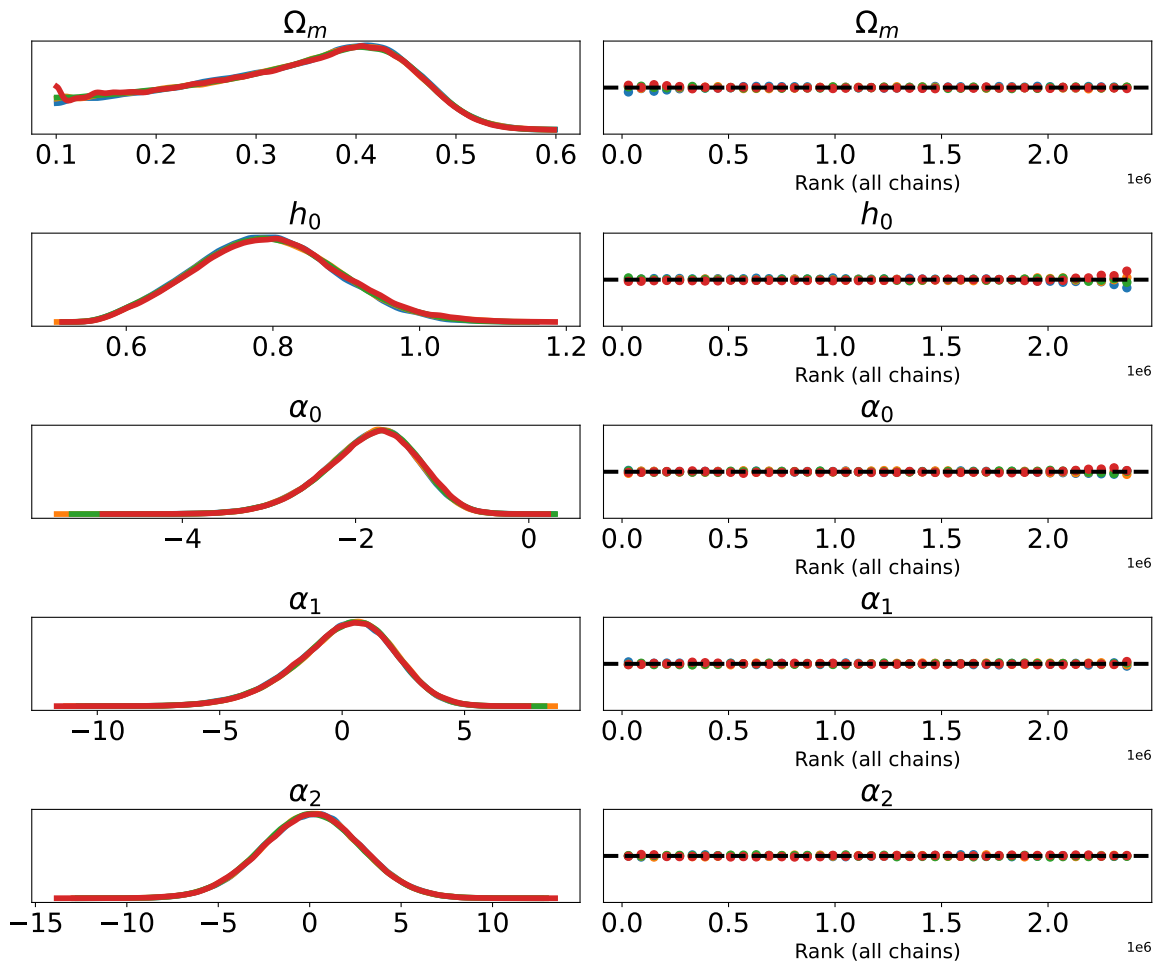


Figure 14: In this figure, the real Hubble parameter data-set is used to generate the plots. As in fig(9) the left column consists of a smoothed histogram, using kernel density estimation of the marginal posteriors of each stochastic random variable. The right-hand column gives the auto-correlation for all the random variables for all the four independent chains, which are depicted with vertical lines.

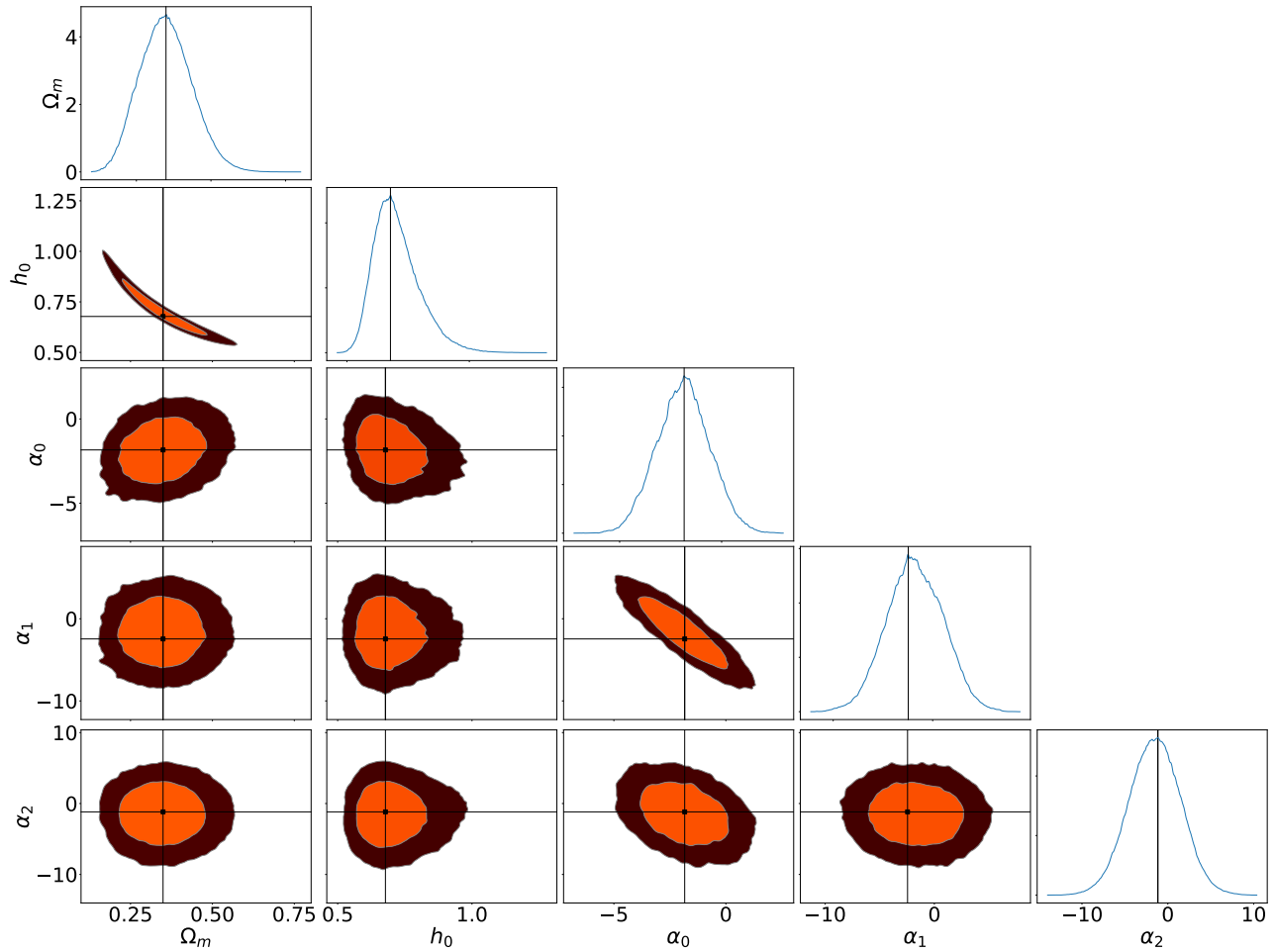


Figure 15: The plot shows the 1σ and 2σ contours for all the parameters along with their marginal probability density plots for the case of real data-set (Zhang *et al.*, 2014; Simon *et al.*, 2005; Moresco *et al.*, 2012; Ratsimbazafy *et al.*, 2017; Moresco, 2015). Constraints on the parameter is done using the Matropolis Hasting algorithm. The first plot of every column shows the marginal probability density plot, which give the maximum evidence of the real Hubble parameter data-set.

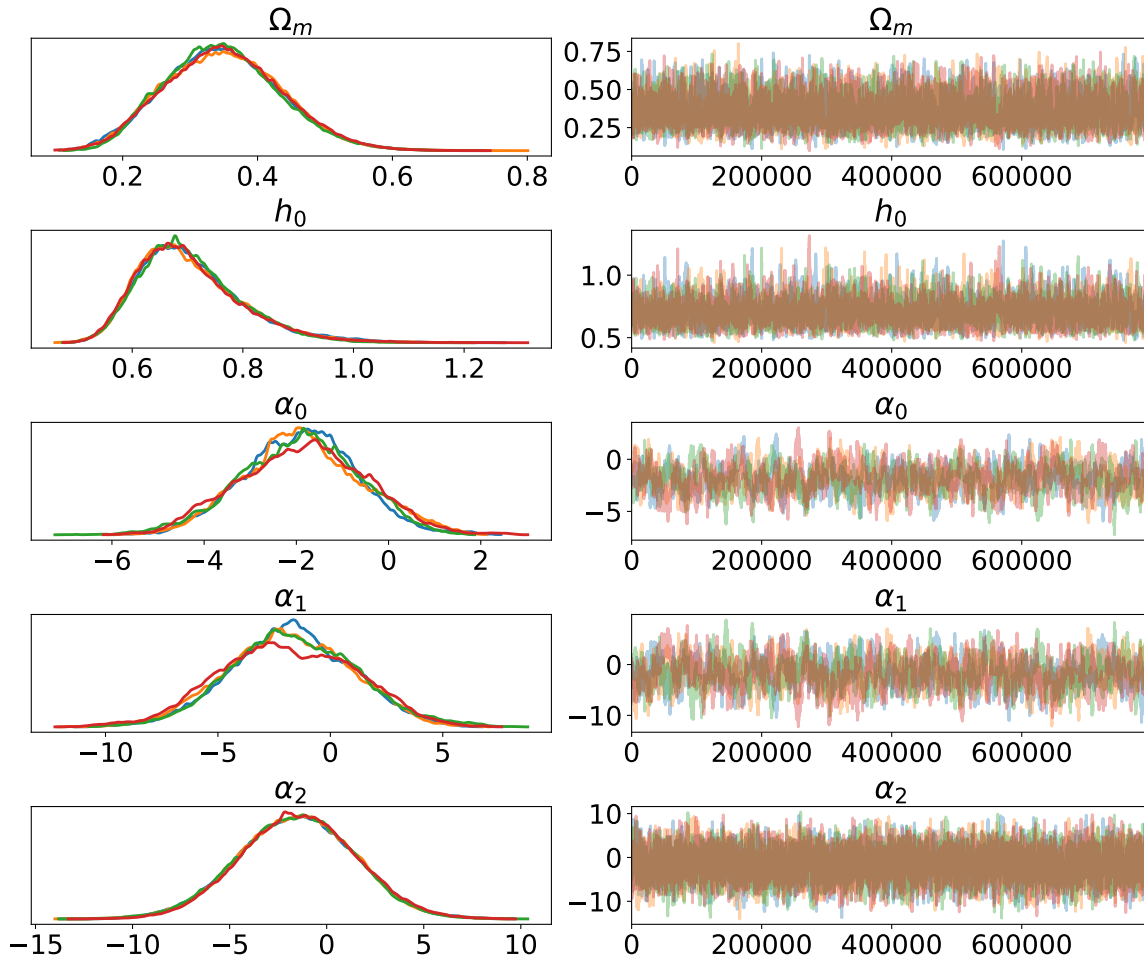


Figure 16: Here we use Matropolis-Hasting algorithm to explore the parameter space created for the model of eqn(1, 2). As in the fig(9), the left consists of a smoothed histogram, using kernel density estimation of the marginal posteriors of each stochastic random variable. These plots are created with $(n_d, M_s) = (600, 800000)$ and all are for the real Hubble parameter data-set. From top to bottom, the random variables are density parameters for matter Ω_m , reduced Hubble constant h_0 , and the parameters of the equation of state of dark energy α_i . The right column contains the samples of the Markov chain plotted in sequential order. There are four MCMC chains that are plotted in different colors.

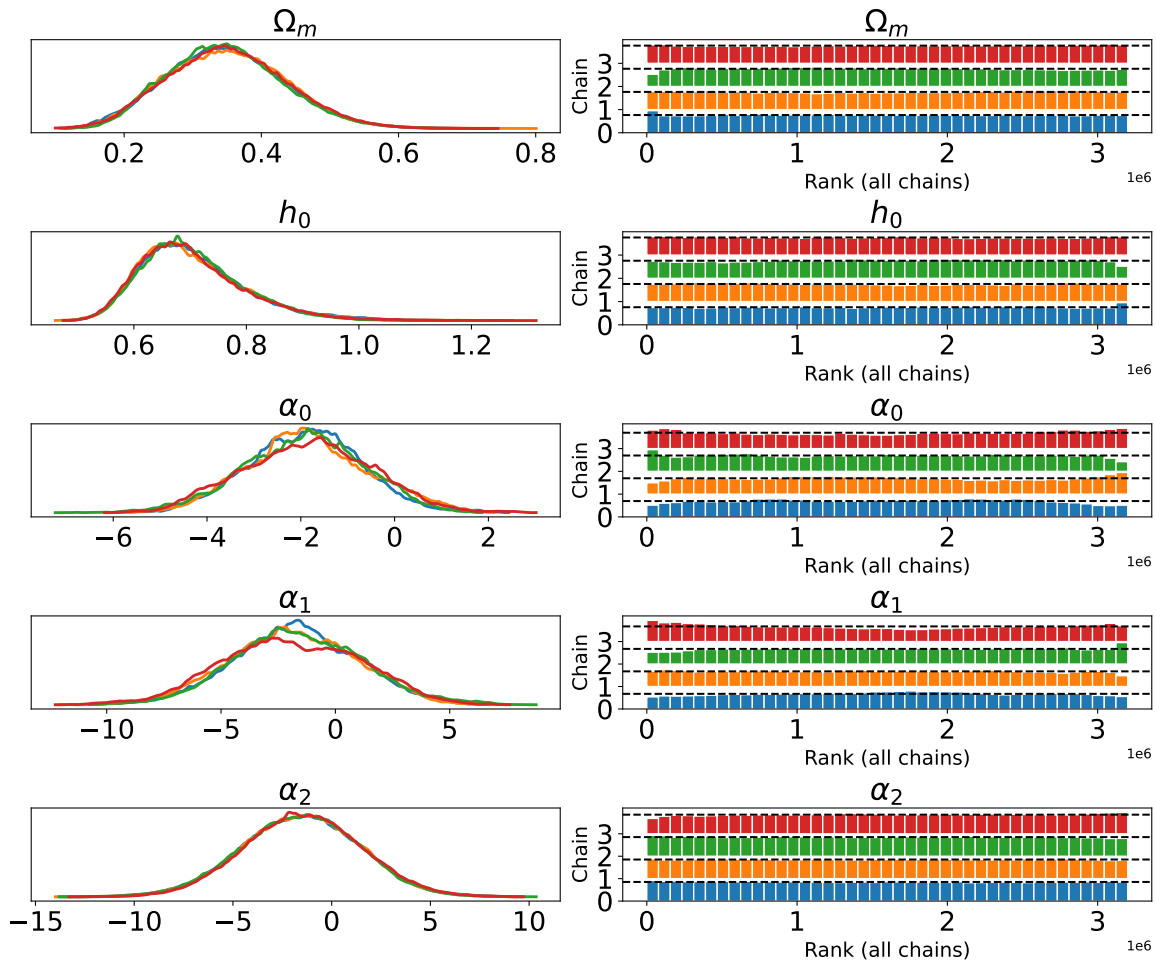


Figure 17: These plots are for the MH algorithm. Smoothed histogram using kernel density estimation of the marginal posteriors of each stochastic random variable. Sequence of the parameters in the plot are same as in the fig(16). The four MCMC chains are plotted in different colors and all are independent of each other.

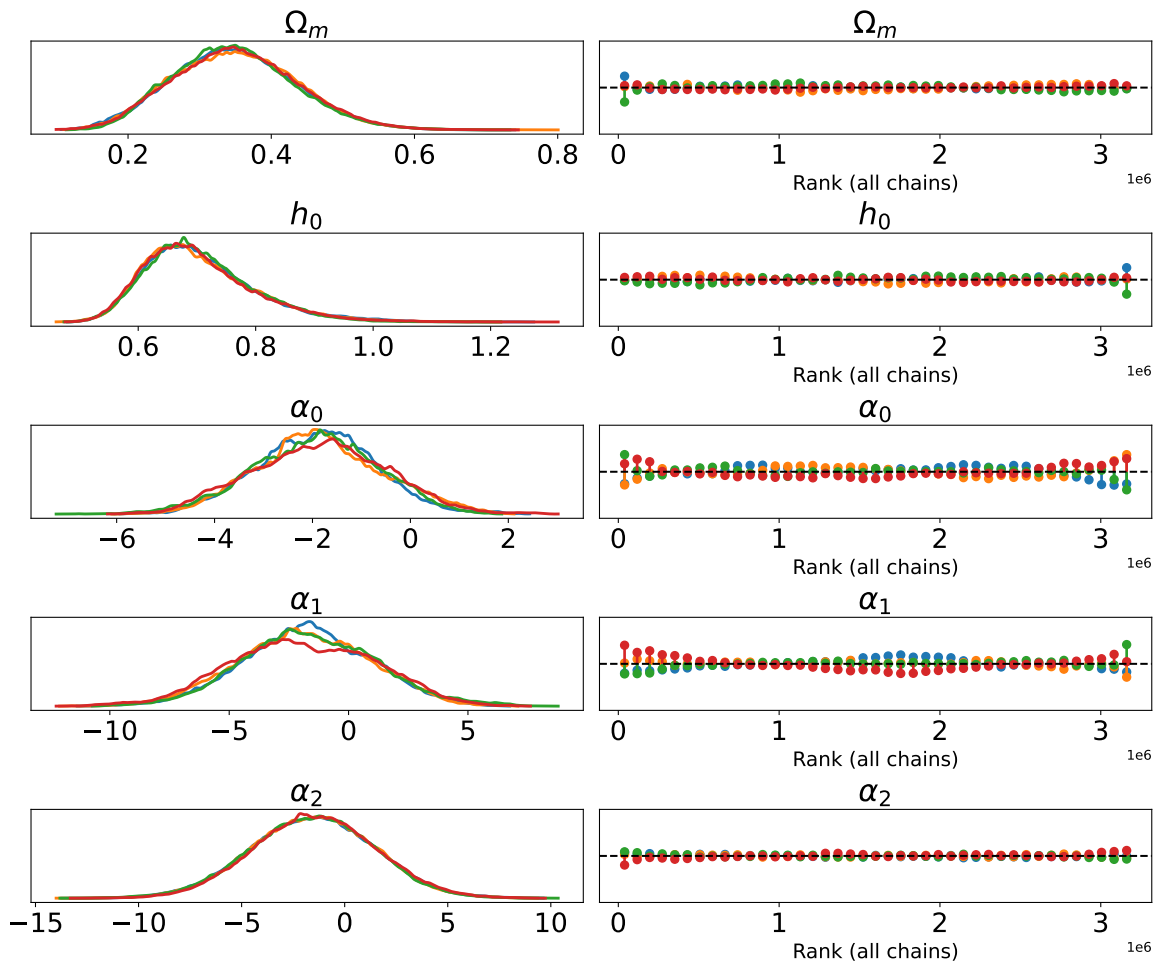


Figure 18: In this figure, the left column consists of a smoothed histogram, using kernel density estimation of the marginal posteriors of each stochastic random variable. The right-hand column gives the auto-correlation for all the random variables for all four independent chains, which are depicted with vertical lines. As in the fig(16,17) these are also for the MH algorithm.

Algo param	MH	NUTS
$m = 3; \Omega_m, h_0$	79.84	82.28
$m = 5; \Omega_m, h_0$	207.20	85.561
$m = 10; \Omega_m, h_0$	259.34	97.31

Table 2: Here, we give the total time taken by Matropolis-Hasting(MH) and NUTS algorithm. In the above table m is the number of EoS parameter, eqn(2). Time taken is shown in the unit of seconds. Each time is the average over 20 identical runs, with the 64 bit x86_64 architecture computer. $(n_d, M_s) = (100, 100)$ for all the runs.

Acknowledgements

We would like to thank J S Bagla for useful suggestions. We would also like to thank PyMC3 team (Salvatier *et al.*, 2016; R Core Team, 2013) for making their software open-source and user-friendly.

Data Availability

The observational data-set used in the analysis is publicly available and duly referred to in the text (Zhang *et al.*, 2014; Simon *et al.*, 2005; Moresco *et al.*, 2012; Ratsimbazafy *et al.*, 2017; Moresco, 2015; Scolnic *et al.*, 2022). The simulated data-set can be created by using the standard Λ CDM model, using eqn(1-6) of the text.

References

Albrecht, A., Bernstein, G., Cahn, R., *et al.* 2006, arXiv e-prints, astro

Alcaniz, J. S., Carvalho, G. C., Bernui, A., Carvalho, J. C., & Benetti, M. 2017, *Fundam. Theor. Phys.*, 187, 11

Arjona, R., & Nesseris, S. 2020, arXiv e-prints, arXiv:2012.12202

Bagla, J. S., Jassal, H. K., & Padmanabhan, T. 2003, *Phys. Rev. D*, 67, 063504

Banerjee, A., Cai, H., Heisenberg, L., *et al.* 2021, *Phys. Rev. D*, 103, L081305

Bellomo, N., Bernal, J. L., Scelfo, G., Raccanelli, A., & Verde, L. 2020, *J. Cosmology Astropart. Phys.*, 2020, 016

Bernal, J. L., Bellomo, N., Raccanelli, A., & Verde, L. 2020, *J. Cosmology Astropart. Phys.*, 2020, 017

Brooks, S. P., & Gelman, A. 1998, *Journal of Computational and Graphical Statistics*, 7, 434

Caldwell, R. R., Dave, R., & Steinhardt, P. J. 1998, *Phys. Rev. Lett.*, 80, 1582

Caldwell, R. R., & Linder, E. V. 2005, *Phys. Rev. Lett.*, 95, 141301

Carnero, A., Sánchez, E., Crocce, M., Cabré, A., & Gaztañaga, E. 2012, *MNRAS*, 419, 1689

Carroll, S. M. 2001, *Living Rev. Rel.*, 4, 1

Carroll, S. M., Press, W. H., & Turner, E. L. 1992, *Annual Review of Astronomy and Astrophysics*, 30, 499

Carvalho, G. C., Bernui, A., Benetti, M., Carvalho, J. C., & Alcaniz, J. S. 2016, *Phys. Rev. D*, 93, 023530

Carvalho, G. C., Bernui, A., Benetti, M., *et al.* 2020, *Astroparticle Physics*, 119, 102432

Chevallier, M., & Polarski, D. 2001, *Int. J. Mod. Phys.*, D10, 213

Chevallier, M., & Polarski, D. 2001, *International Journal of Modern Physics D*, 10, 213

Clarkson, C., & Zunckel, C. 2010, *Phys. Rev. Lett.*, 104, 211301

Coble, K., Dodelson, S., & Frieman, J. A. 1997, *Phys. Rev. D*, 55, 1851

- Copeland, E. J., Liddle, A. R., & Wands, D. 1998, *Phys. Rev.*, D57, 4686
- Copeland, E. J., Sami, M., & Tsujikawa, S. 2006, *Int. J. Mod. Phys.*, D15, 1753
- Cowles, M. K., & Carlin, B. P. 1996, *Journal of the American Statistical Association*, 91, 883
- Crittenden, R. G., Pogosian, L., & Zhao, G.-B. 2009, *JCAP*, 0912, 025
- de Carvalho, E., Bernui, A., Carvalho, G. C., Novaes, C. P., & Xavier, H. S. 2018, *J. Cosmology Astropart. Phys.*, 2018, 064
- Deng, H.-K., & Wei, H. 2018, *European Physical Journal C*, 78, 755
- Di Valentino, E., Melchiorri, A., Linder, E. V., & Silk, J. 2017, *Phys. Rev.*, D96, 023523
- Ellis, J. 2003, *Philosophical Transactions of the Royal Society of London A: Mathematical, Physical and Engineering Sciences*, 361, 2607
- Frieman, J. A., Turner, M. S., & Huterer, D. 2008, *Annual Review of Astronomy and Astrophysics*, 46, 385
- Gelman, A., & Rubin, D. B. 1992, *Statistical Science*, 7, 457
- Gong, Y.-G., & Wang, A. 2007, *Phys. Rev.*, D75, 043520
- Hart, L., & Chluba, J. 2019, *arXiv e-prints*, arXiv:1912.04682
- . 2022a, *MNRAS*, 510, 2206
- . 2022b, *MNRAS*, 510, 2206
- Hoffman, M. D., & Gelman, A. 2011, *arXiv e-prints*, arXiv:1111.4246
- Hojjati, A., Zhao, G.-B., Pogosian, L., *et al.* 2012, *Phys. Rev. D*, 85, 043508
- Huterer, D., & Cooray, A. 2005, *Phys. Rev. D*, 71, 023506
- Huterer, D., & Peiris, H. V. 2007, *Phys. Rev.*, D75, 083503
- Huterer, D., & Starkman, G. 2003, *Phys. Rev. Lett.*, 90, 031301
- Ishida, E. E. O., & de Souza, R. S. 2011, *A&A*, 527, A49
- Jassal, H. K. 2009, *Phys. Rev.*, D79, 127301
- Jassal, H. K., Bagla, J. S., & Padmanabhan, T. 2005, *Mon. Not. Roy. Astron. Soc.*, 356, L11
- Jiao, K., Borghi, N., Moresco, M., & Zhang, T.-J. 2023, *ApJS*, 265, 48
- Jimenez, R., Moresco, M., Verde, L., & Wandelt, B. D. 2023, *arXiv e-prints*, arXiv:2306.11425
- Kendall. 1938, *Biometrika*, 30, 81
- Kreyszig, E., Kreyszig, H., & Norminton, E. J. 2011, *Advanced engineering mathematics*, tenth edn. (Hoboken, N.J.: Wiley)
- Lee, B.-H., Lee, W., Ó Colgáin, E., Sheikh-Jabbari, M. M., & Thakur, S. 2022, *J. Cosmology Astropart. Phys.*, 2022, 004
- Linder, E. V. 2003, *Phys. Rev. Lett.*, 90, 091301
- Linder, E. V. 2003, *Phys. Rev. Lett.*, 90, 091301
- Linder, E. V. 2006, *Phys. Rev.*, D73, 063010
- Linder, E. V. 2008, *Reports on Progress in Physics*, 71, 056901
- Linder, E. V. 2008, *Gen. Rel. Grav.*, 40, 329
- Liu, Z.-E., Qin, H.-F., Zhang, J., Zhang, T.-J., & Yu, H.-R. 2019, *Physics of the Dark Universe*, 26, 100379
- Liu, Z.-E., Yu, H.-R., Zhang, T.-J., & Tang, Y.-K. 2016, *Phys. Dark Univ.*, 14, 21
- Miranda, V., & Dvorkin, C. 2018, *Phys. Rev. D*, 98, 043537
- Moresco, M. 2015, *MNRAS*, 450, L16
- Moresco, M., Jimenez, R., Verde, L., Cimatti, A., & Pozzetti, L. 2020, *ApJ*, 898, 82
- Moresco, M., Verde, L., Pozzetti, L., Jimenez, R., & Cimatti, A. 2012, *JCAP*, 1207, 053
- Mukherjee, A. 2016, *Mon. Not. Roy. Astron. Soc.*, 460, 273
- Nair, R., & Jhingan, S. 2013, *J. Cosmology Astropart. Phys.*, 2013, 049
- Nesseris, S., & García-Bellido, J. 2013, *Phys. Rev. D*, 88, 063521
- Nesseris, S., & Perivolaropoulos, L. 2004, *Phys. Rev. D*, 70, 043531

- . 2005, *Phys. Rev. D*, 72, 123519
- . 2007, *J. Cosmology Astropart. Phys.*, 2007, 018
- Nunes, R. C., Yadav, S. K., Jesus, J. F., & Bernui, A. 2020, *MNRAS*, 497, 2133
- Padmanabhan, T. 2002, *Phys. Rev. D*, 66, 021301
- . 2003, *Phys. Rept.*, 380, 235
- Peebles, P. J. E., & Ratra, B. 2003, *Rev. Mod. Phys.*, 75, 559, [592(2002)]
- Planck Collaboration, Aghanim, N., Akrami, Y., *et al.* 2018, arXiv e-prints, arXiv:1807.06209
- R Core Team. 2013, *R: A Language and Environment for Statistical Computing*, R Foundation for Statistical Computing, Vienna, Austria
- Rajvanshi, M. P., & Bagla, J. S. 2019, *Journal of Astrophysics and Astronomy*, 40, 44
- Ratra, B., & Peebles, P. J. E. 1988, *Phys. Rev.*, D37, 3406
- Ratsimbazafy, A. L., Loubser, S. I., Crawford, S., *et al.* 2017, *Mon. Not. Roy. Astron. Soc.*, 467, 3239
- Riess, A. G., Casertano, S., Yuan, W., *et al.* 2021, *ApJ*, 908, L6
- Sahni, V., & Starobinsky, A. 2000, *International Journal of Modern Physics D*, 9, 373
- Salvatier, J., Wiecki, T. V., & Fonnesbeck, C. 2016, *PeerJ Computer Science*, 2, e55
- Sánchez, E., Carnero, A., García-Bellido, J., *et al.* 2011, *MNRAS*, 411, 277
- Sangwan, A., Tripathi, A., & Jassal, H. K. 2018, arXiv e-prints, arXiv:1804.09350
- Scolnic, D., *et al.* 2022, *Astrophys. J.*, 938, 113
- Sharma, R., Mukherjee, A., & Jassal, H. K. 2020, arXiv e-prints, arXiv:2004.01393
- Simon, J., Verde, L., & Jimenez, R. 2005, *Phys. Rev.*, D71, 123001
- Singh, A., Sangwan, A., & Jassal, H. K. 2019, *JCAP*, 1904, 047
- Stern, D., Jimenez, R., Verde, L., Kamionkowski, M., & Stanford, S. A. 2010, *J. Cosmology Astropart. Phys.*, 2010, 008
- Tsujikawa, S. 2013, *Classical and Quantum Gravity*, 30, 214003
- Turner, M. S., & White, M. 1997, *prd*, 56, R4439
- Uddin, S. A., Burns, C. R., Phillips, M. M., *et al.* 2023, arXiv e-prints, arXiv:2308.01875
- Vagnozzi, S., Dhawan, S., Gerbino, M., *et al.* 2018, *Phys. Rev. D*, 98, 083501
- Vehtari, A., Gelman, A., Simpson, D., Carpenter, B., & Bürkner, P.-C. 2019, arXiv e-prints, arXiv:1903.08008
- Verde, L., Protopapas, P., & Jimenez, R. 2013, *Physics of the Dark Universe*, 2, 166
- Weinberg, S. 1989, *Rev. Mod. Phys.*, 61, 1
- York, D. G., Adelman, J., Anderson, John E., J., *et al.* 2000, *AJ*, 120, 1579
- Zhang, C., Zhang, H., Yuan, S., *et al.* 2014, *Research in Astronomy and Astrophysics*, 14, 1221
- Zheng, W., & Li, H. 2017, *Astropart. Phys.*, 86, 1
- Zlatev, I., Wang, L.-M., & Steinhardt, P. J. 1999, *Phys. Rev. Lett.*, 82, 896